Retrieval of NO₂ profiles from three years of Pandora MAX-DOAS measurements in Toronto, Canada

Ramina Alwarda[1,2], Kristof Bognar[3], Xiaoyi Zhao[2], Vitali Fioletov[2], Jonathan Davies[2], Sum Chi Lee[2],

5   Debora Griffin[2], Alexandru Lupu[2], Udo Frieß[4], Alexander Cede[5,6], Yushan Su[7], Kimberly Strong[1]

[1]Department of Physics, University of Toronto, Toronto, Canada
[2]Air Quality Research Division, Environment and Climate Change Canada, Toronto, Canada
[3]3vGeomatics, Vancouver, Canada
[4]Institute of Environmental Physics, Heidelberg University, Heidelberg, Germany
10 [5]NASA Goddard Space Flight Center, Greenbelt, USA
[6]LuftBlick, Innsbruck, Austria
[7]Ontario Ministry of the Environment, Conservation and Parks, Toronto, Canada

Correspondence to: Ramina Alwarda (ramina.alwarda@mail.utoronto.ca)

Abstract. The purpose of this work is to derive new NO₂ vertical profiling data products from Pandora spectrometers and

15 investigate the factors contributing to the bias of this dataset relative to established ground-based and spaceborne datasets. Possible applications of the NO₂ vertical profile dataset include air quality monitoring and satellite validation studies. We explore the application of the optimal estimation method to Pandora multi-axis differential optical absorption spectroscopy (MAX-DOAS) measurements to retrieve vertical profile information for nitrogen dioxide (NO₂). We use the Heidelberg Profile (HeiPro) retrieval algorithm to derive, for the first time, NO₂ profiles and partial columns (0–4 km) from Pandora MAX-DOAS

20 measurements from 2018–2020 at Downsview, a suburban neighbourhood in the north end of Toronto, Canada that is subject to local traffic emissions and urban influences. Validation of the new dataset was done via comparison with official Pandora direct-Sun measurements, in situ observations, satellite data, and an air quality forecasting model. We find that, for tropospheric partial column comparisons, the HeiPro dataset has a positive mean relative bias to Pandora direct-Sun (61% ± 9.7%) and TROPOMI (41% ± 47%) observations, as well as the GEM-MACH model output (61% ± 7.5%), with similar

25 seasonal and diurnal cycles in the bias with Pandora direct-Sun and GEM-MACH. Contributing factors to the large bias of HeiPro to Pandora direct-Sun were investigated, and NO₂ heterogeneity, combined with differences between direct-Sun and multi-axis viewing geometries, was found to contribute a maximum of 52% of the total relative bias during morning measurement times. For surface NO₂ comparisons, we find that HeiPro measurements capture the magnitude and diurnal variability of surface NO₂ reasonably well (mean relative bias to in situ surface NO₂: −8.9% ± 7.6%) but are low-biased

30 compared to GEM-MACH (mean relative bias: −36% ± 2.4%). Compared to HeiPro, the GEM-MACH model profiles are high-biased in the lower boundary layer and low-biased in the free troposphere.

1 Introduction

Nitric oxide (NO) and nitrogen dioxide (NO_2), together comprising NO_x, play important roles in air quality, tropospheric chemistry, and stratospheric ozone (O_3) chemistry. In the troposphere, NO_x is primarily emitted from fossil fuel combustion and nitrogen fertilizers and has a near-surface peak in the profile shape in polluted regions; additionally, it is emitted from natural sources such as lightning and biomass burning (e.g., ECCC 2016; Murray, 2016). The photolysis of NO_2 rapidly contributes to the production of O_3 and therefore photochemical smog formation. NO_2 also plays a more direct role in air quality as it has toxic biological effects at high concentrations and has been linked to negative health outcomes such as asthma exacerbations (ECCC, 2016). Tropospheric NO_2 has a large spatiotemporal variability and this can be attributed to its short lifetime, variability of emissions, and meteorological variations (Beirle et al., 2003).

Due to its role in various atmospheric processes and impact on air quality, it is important to continuously monitor NO_2 and its spatiotemporal variability. Surface NO_2 is measured using in situ photolytic conversion/chemiluminescence as part of Canada's Air Quality Health Index (AQHI, Stieb et al., 2008) along with surface O_3 and surface fine particulate matter with diameter < 2.5 microns (PM2.5). While in situ instruments provide surface measurements with high temporal resolution, such measurements are spatially limited both in geographic extent and altitude. Ground-based remote sensing measurements address the latter limitation by measuring NO_2 throughout the troposphere and stratosphere and are used in air quality and satellite validation studies (e.g., Ma et al., 2013; Griffin et al., 2019; Zhao et al., 2019, 2020; Verhoelst et al., 2021). Non-geostationary satellite instruments, on the other hand, address spatial limitations from ground-based monitoring and provide global coverage. A suite of UV-visible satellite instruments has monitored NO_2 columns since 1995, beginning with the Global Ozone Monitoring Experiment (GOME, Burrows et al., 1999) and more recently, the TROPOspheric Monitoring Instrument (TROPOMI) onboard the European Space Agency's Sentinel-5 Precursor (S5P) satellite. While such satellite instruments provide global coverage, the temporal frequency of at any location is limited, which hinders insight into the spatiotemporal variation of NO_2 on large scales. The recent additions of geostationary satellite instruments such as the Tropospheric Emissions: Monitoring of Pollution (TEMPO, Zoogman et al., 2017) and the Geostationary Environmental Monitoring Spectrometer (GEMS, Kim et al., 2020) address this limitation of low-Earth satellite orbits. Thus, in situ, ground-based, and spaceborne measurements all contribute to our understanding of the spatiotemporal variability of NO_2.

Ground-based UV-visible spectra are usually analysed using Differential Optical Absorption Spectroscopy (DOAS, Platt and Stutz, 2008). These measurements include zenith-scattered-light DOAS (ZSL-DOAS), which is most sensitive to the stratospheric column, multi-axis DOAS (MAX-DOAS), which is most sensitive to the tropospheric column, and direct-Sun (DS), which measures the total column with equal sensitivity to the troposphere and stratosphere. One such ground-based instrument that performs routine direct-Sun, zenith-sky, and multi-axis measurements of the atmosphere is the Pandora UV-visible spectrometer (Herman et al., 2009). Pandora instruments are distributed globally as part of the Pandonia Global

65   Network (PGN), an international collaboration led by the National Aeronautics and Space Administration (NASA), European Space Agency (ESA), the US Environmental Protection Agency (US-EPA), and the Korean National Institute of Environmental Research (NIER), which provides standardized high-quality datasets, such as direct-Sun NO_2 total columns, for various purposes including satellite validation and air quality assessments (e.g., Zhao et al., 2022).

70   Additionally, Pandora MAX-DOAS spectra can be used to retrieve vertical profiles of trace gases in the lower troposphere, for example by using the optimal estimation method (OEM), a maximum a posteriori profile inversion algorithm which is based on Bayesian statistics and provides a robust error analysis (Rodgers, 2000; Frieß et al., 2019). Utilizing a MAX-DOAS NO_2 dataset is advantageous because it provides sensitivity to tropospheric absorbers, profile information, increased temporal resolution compared to spaceborne measurements, horizontal distribution of NO_2 surrounding a measurement site
75   (Dimitropoulou et al., 2020), and a horizontal resolution that is more suited for assessing model performance compared to in situ data (Blechschmidt et al., 2020). NO_2 profiles from MAX-DOAS measurements are also a useful tool for aiding in satellite retrieval algorithms and validation; previous studies have utilized NO_2 profiles derived from MAX-DOAS data as inputs for the TROPOMI retrieval algorithm to reduce the systematic underestimation in the satellite data compared to ground-based data (e.g., Dimitropoulou et al., 2020). Partial columns of NO_2 from MAX-DOAS data have also been used in ground-based
80   validation of spaceborne measurements, whereby satellite tropospheric NO_2 is typically biased low to ground-based MAX-DOAS NO_2 in polluted regions (e.g., Pinardi et al., 2020; Verhoelst et al., 2021). Satellite measurements rely on ground-based data to continuously improve satellite algorithms and understand the bias that exists between spaceborne and ground-based measurements as a function of location, especially due to the difficulty in implementing location-specific a priori NO_2 profiles in satellite retrieval algorithms (Verhoelst et al., 2021). In addition to OEM, there are various other retrieval techniques that
85   convert MAX-DOAS measurements to NO_2 profiles and subsequent data products. For example, Pandora MAX-DOAS spectra can be used to retrieve NO_2 vertical profiles, tropospheric columns, and surface values using an L2 Air-Ratio Sky Algorithm developed by Elena Spinei and the PGN (see PGN software manual v1.8 available at https://www.pandonia-global-network.org/home/documents/manuals/ for further information, last access 13 September 2024). Comparisons of these PGN sky algorithm data products with other datasets at the measurement site in this study will be the subject of a future study.

90

    While OEM has been applied to Pandora MAX-DOAS data in a study by Nowlan et al. (2018) that compared aircraft retrievals of NO_2 to ground-based MAX-DOAS and direct-Sun Pandora measurements for an eleven-day period, it has not yet been applied to Pandora MAX-DOAS observations for extended periods of time. A longer intercomparison period would enable investigations of annual and seasonal trends compared to other NO_2 datasets, especially comparing Pandora MAX-
95   DOAS to direct-Sun observations. Previous comparisons between NO_2 observations of MAX-DOAS to direct-Sun are limited but would be useful in addressing the difference in the relative biases of multi-axis and direct-Sun observations to satellite measurements. For example, Pinardi et al. (2020) found a bias of 10–15% in the ground-based MAX-DOAS NO_2 columns compared to direct-Sun tropospheric columns from the same station, but such comparisons were during the overpass times of

Atmospheric
Measurement
Techniques
Discussions

Open Access

EGU

the two satellites in the study. The relative bias was attributed to NO_2 heterogeneity as well as the differences in airmasses

100   measured by the direct-Sun and multi-axis geometries. Performing NO_2 comparisons of MAX-DOAS to direct-Sun throughout

the day would be an important consideration for the validation of geostationary satellite NO_2 measurements, since both are

used for the validation of spaceborne tropospheric NO_2 (e.g., Verhoelst et al., 2021).

Therefore, due to the advantages of obtaining NO_2 profiles, as well as the limited studies comparing MAX-DOAS to

105   direct-Sun NO_2, the aim of this work is to derive NO_2 profiles from Pandora MAX-DOAS measurements using OEM and to

assess the quality of the dataset by comparison to established datasets. We present, for the first time, a three-year dataset of 0–

4 km NO_2 profiles from 2018–2020 at Downsview, a Pandora measurement site in the north part of Toronto, Ontario, Canada,

located in a suburban area subject to local traffic emissions and urban influences. Figure 1 shows the 2018–2020 TROPOMI

tropospheric NO_2 field at the measurement site and surrounding region. To our knowledge, this work is the first study to apply

110   the optimal estimation method to Pandora MAX-DOAS data to retrieve a multi-year NO_2 profile dataset. We assess the biases

and contributing factors to the biases between the OEM-based Pandora dataset versus (1) standard measurements comprising

Pandora direct-Sun and TROPOMI tropospheric columns as well as in situ surface NO_2, and (2) profiles, partial columns, and

surface NO_2 from the Global Environmental Multiscale–Modelling Air-quality and Chemistry (GEM-MACH) high-resolution

regional air quality forecast model. Where possible, we quantify the contributing factors to the biases and assess the impact of

115   spatial heterogeneity on the biases. The resulting OEM-based Pandora NO_2 profile dataset can used to assess spatiotemporal

NO_2 heterogeneity around the measurement site as well as any biases between spaceborne and ground-based NO_2 at the
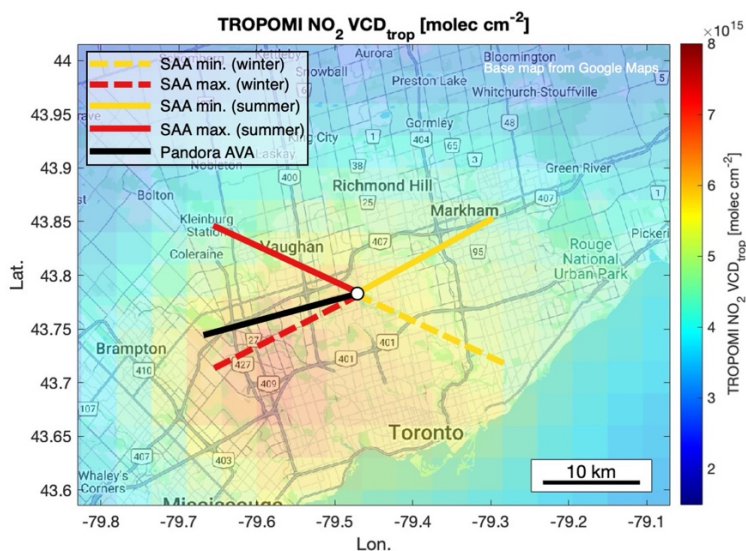
measurement site.

Figure 1: A map (© Google Maps) of the measurement site (Downsview, white circle) and surrounding

120   **Greater Toronto Area masked by the TROPOMI pixel-averaged tropospheric NO_2 field from 2018–2020. The color**

bar indicates the NO₂ tropospheric column in molec cm^{-2}. Solid and dashed lines represent the minimum (yellow) and maximum (red) solar azimuth angle (SAA) during summer and winter, respectively. The solid black line represents the Pandora instrument's multi-axis azimuth viewing angle (AVA) of 255°.

125   The paper is organized as follows: Section 2 describes the various instruments, algorithms, and models used in this study, as well as the data filtering and co-location criteria that were applied. In Section 3, the quality of the OEM-based Pandora dataset is assessed by comparing it with Pandora direct-Sun and TROPOMI tropospheric columns as well as GEM-MACH partial columns. Section 4 presents the surface NO₂ volume mixing ratio (VMR) comparisons among the OEM-based Pandora dataset, in situ data from the National Air Pollution Surveillance (NAPS) monitoring program, and GEM-MACH data, as well

130   as the comparisons between Pandora OEM and GEM-MACH NO₂ profiles. Seasonal and diurnal trends are examined where possible, and the causes of differences among the measurements are investigated. Finally, Section 5 summarizes the implications and conclusions.

2 Methods: Instruments, Retrieval Algorithms, and Models

An overview of the instruments and corresponding datasets used in this study is presented in Fig. 2. Section 2.1

135   describes the three instruments: the Pandora spectrometer, TROPOMI, and the photolytic conversion/chemiluminescence in situ sensor. Section 2.2 discusses the retrieval algorithms that were used to convert Pandora direct-Sun spectra to tropospheric columns and Pandora MAX-DOAS data to profiles. Lastly, Section 2.3 focuses on the models used in this work, both auxiliary models used in producing other datasets (Pratmo and ERA5) and the model that contributed an additional NO₂ comparison (i.e., GEM-MACH).
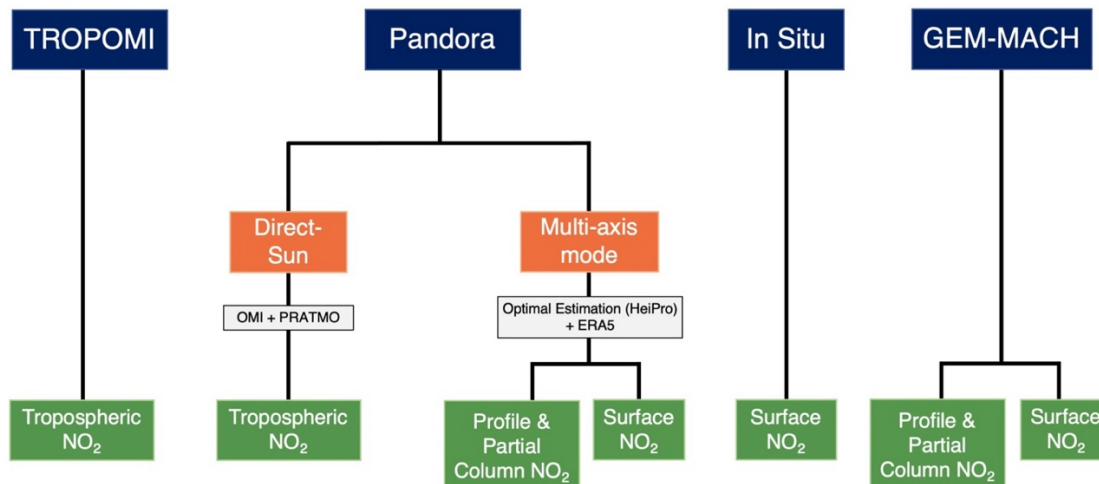
140

Figure 2: Overview of the NO₂ data products used in this study. The blue boxes indicate the instrument or model, the orange boxes indicate Pandora viewing geometries, and the green boxes indicate the final data products.

Atmospheric
Measurement
Techniques
Discussions
EGU
Open Access

2.1 Instruments

2.1.1 Pandora UV-Visible Spectrometer

145   Pandora instruments utilize a temperature-stabilized Czerny-Turner spectrometer with a grating of 1200 gr/mm and a back-thinned charge-coupled device (CCD) detector to record spectra between 280–530 nm with a spectral resolution of 0.6 nm. All Pandora NO_2 data products presented in this work were obtained from Pandora no. 103 (P103) located on the rooftop of the Environment and Climate Change Canada (ECCC) five-storey building at Downsview (43.78 °N, 79.47 °W, 186 m a.s.l.) in Toronto, Canada. This building is located in a suburban region with several nearby roads. P103 operates in direct-

150   Sun, zenith-sky, and multi-axis viewing geometries during the sunlit period. Direct-Sun and multi-axis data products from P103 from February 2018 to June 2020 were used in this study. Further details on the direct-Sun retrieval technique are discussed in Section 2.2.1, while a preface to the multi-axis viewing geometry is provided below prior to being further discussed in Section 2.2.2.

155   The multi-axis viewing geometry can provide vertical information from tropospheric absorbers by measuring scattered sunlight at various elevation viewing angles (EVAs) of the instrument. P103 performs both 'long' and 'short' scans in an alternating manner, with an azimuth viewing angle of 255° (see Fig. 1). Long scans consist of EVAs of 1°, 2°, 3°, 5°, 8°, 10°, 15°, 20°, 30°, 40°, 50°, and 90° and short scans consist of EVAs of 1°, 2°, 15°, 30°, and 90°. The resulting multi-axis spectra (i.e., corrected Level 1 data, data file version: smca1c1p1-7) were obtained from the PGN. Utilizing the DOAS

160   technique, spectral fitting to the ratio of two spectra, with one spectrum at each EVA and the other at a 90° reference EVA, is performed to retrieve the differential slant column density (dSCD) of NO_2 at each EVA. This is achieved using the QDOAS software (https://uv-vis.aeronomie.be/software/QDOAS/, last access: 16 April 2024), developed by the Royal Belgian Institute for Space Aeronomy (Danckaert et al., 2017), with fitting parameters outlined in Appendix A of Kreher et al. (2020). NO_2 and oxygen collision complex (O_4) dSCDs were retrieved in both the ultraviolet (UV, 338–370 nm) and visible (vis, 425–490 nm)

165   windows. Following this, NO_2 dSCDs were converted to profiles using the maximum a posteriori optimal estimation method as implemented in the Heidelberg Profile Retrieval algorithm (HeiPro, Frieß et al., 2011; Yilmaz, 2012), which is discussed in Section 2.2.2.

2.1.2 TROPOMI

        The TROPOMI instrument measures nadir solar UV-visible radiance in a sun-synchronous orbit at an altitude of 817

170   km and a local overpass time of 13:30 LST. The TROPOMI instrument provides spaceborne NO_2 measurements at a horizontal resolution of 3.5 km × 5.5 km (3.5 km × 7.5 km prior to August 2019). The DOAS technique is used to convert UV-visible spectra to NO_2 slant column densities (SCDs). Following this, a chemical transport model (TM5-MP) assimilates the SCDs to NO_2 vertical profiles, from which a stratospheric SCD is determined. Finally, air mass factors (AMFs, which are based on surface albedo, NO_2 profile shape, etc.) are used to obtain a tropospheric column. Details about the instrument and NO_2

Atmospheric
Measurement
Techniques
Discussions
EGU
Open Access

175 retrieval scheme can be found in van Geffen et al. (2020). The TROPOMI tropospheric columns used in this work are from processor version 2.3.1 (van Geffen et al., 2022). We used tropospheric NO_2 data product quality assurance values (qa_value) ≥ 0.75 to exclude retrievals with very cloudy scenes. Only TROPOMI pixels that were within 10 km of the Pandora measurement site, i.e., the ECCC building at Downsview, and within ± 10 minutes of the Pandora MAX-DOAS measurement time (Zhao et al., 2020) were included in the comparisons.

2.1.3 In situ Measurements

180 The in situ instrument (Thermo 42i) at the Toronto North site, i.e., the Pandora measurement site, monitors surface NO_2 under the NAPS Program and is located near a major road. Horizontally, it is located 100 m away from the Pandora instrument; vertically, it has an air intake inlet that is 4 m above ground level and 11 m below the Pandora instrument. It utilizes the photolytic conversion/chemiluminescence technique to measure NO_2 with a precision of 0.4 ppb. The NO_2 data collected at the Toronto North site was provided on an hourly-averaged timescale and had undergone final validation by the Ontario
185 Ministry of the Environment, Conservation and Parks.

2.2 Pandora Retrieval Algorithms

2.2.1 Pandora Direct-Sun

The standard PGN total column NO_2 data product is obtained from Pandora direct-Sun spectra using Total Optical
190 Absorption Spectroscopy (TOAS, Cede, 2021). Direct-Sun spectra in the 400–440 nm range are fitted with cross-sections of NO_2 and O_3, and a fourth-order polynomial to produce SCDs of NO_2. Following this, NO_2 SCDs are converted to vertical column densities (VCDs or total columns) using geometric AMFs (Herman et al., 2009). Because the focus of this work is on tropospheric NO_2 intercomparisons, the resulting NO_2 VCDs were converted to tropospheric NO_2 columns by subtracting the stratospheric NO_2 columns obtained from the Ozone Monitoring Instrument (OMI, NASA standard product version 3.0 level
195 2, Krotkov et al., 2017) onboard the Aura satellite. Due to the diurnal variation of NO_2, and the satellite's overpass time of 13:30 local time (LT), a photochemical box model (Pratmo, discussed further in Section 2.3.1) was used to calculate stratospheric NO_2 at various Pandora measurement times throughout the day. The Pandora direct-Sun NO_2 VCDs are obtained from the PGN (https://data.pandonia-global-network.org/Downsview/Pandora103s1/, file version: rnvs1p1-7, last access: 16 April 2024) and only high-quality data (i.e., L2 flags of 0 and 10) were used. The Pandora direct-Sun (from here on, Pandora-
200 DS) tropospheric NO_2 data were averaged to obtain hourly means for comparison with the other datasets.

2.2.2 HeiPro

HeiPro was used to convert Pandora dSCDs of NO_2 at various EVAs to NO_2 profiles from 0–4 km. HeiPro is an optimal estimation method (Rodgers, 2000) that utilizes a forward model (a radiative transfer model or RTM, here being SCIATRAN version 2.2, Rozanov et al., 2005), to simulate dSCDs based on a priori NO_2 profile information and additional

Atmospheric
Measurement
Techniques
Discussions

205 parameters such as aerosol extinction, aerosol optical properties, surface albedo, and temperature. Exponentially decreasing aerosol extinction and NO_2 profiles with scale heights of 1 km and column values of 0.18 (aerosol optical depth, AOD) and 9×10^{15} molec cm^{-2} (NO_2) were used as a priori information in the HeiPro simulation. Additional a priori information utilized by HeiPro were pressure and temperature profiles from ERA5 reanalysis data (discussed further in Section 2.3.2). For the aerosol retrievals, a single scattering albedo value of 0.92 and asymmetry factor of 0.68 were used. For all retrievals, a surface

210 albedo value of 0.06 was used, and correlation matrices with a variance of 50% and correlation length of 200 m were used.

Given these settings, a cost function is used to assess the difference between the dSCDs simulated by the RTM and the measured dSCDs while accounting for additional a priori constraints. The Levenberg–Marquardt algorithm is then used to iteratively find the minimum of the cost function. At this minimum, the most probable atmospheric state or the maximum *a*

215 *posteriori* estimate (MAP) is then taken to be the NO_2 profile. HeiPro utilizes a two-step approach: prior to each NO_2 profile retrieval, aerosol extinction profiles are retrieved based on O_4 dSCDs; these are subsequently used as inputs for the NO_2 profile retrievals. Profiles were retrieved separately for UV and visible scans, with RTM wavelengths of 360 nm for O_4-UV and NO_2-UV, 477 nm for O_4-vis, and 460 nm for NO_2-vis. Full details about the HeiPro algorithm can be found in Frieß et al. (2006, 2011). The profile grid is from 0–4 km, with a vertical resolution of 200 m. Therefore, the NO_2 concentration for the 0–200 m

220 grid level represents the average throughout this range, i.e., the concentration at 100 m. The HeiPro 'surface' concentration reported in this study is then obtained by extrapolating the VMR at the 0–200 m grid level to 0 m for each individual profile.

Additionally, only the long multi-axis scans (see Section 2.1.1 for list of EVAs) recorded in the UV window, together termed the 'long UV' scans, were incorporated in this work as they have the most reliable results. We found the HeiPro long

225 UV results to be better suited for this study for the following reasons: (1) as expected, the degrees of freedom for signal (DOFS), which represents the number of independent pieces of information associated with the retrieval of each profile, are greater for the long scans (2.35 and 3.13 for UV and vis, respectively) compared to the short scans (2.03 and 2.75 for UV and vis, respectively), see Fig. A1 (in Appendix A). (2) The root-mean-square (RMS) residuals are reduced for the long scans (5.45×10^{14} and 2.99×10^{14} for UV and vis) compared to the short scans (RMS: 7.51×10^{14} and 3.49×10^{14} for UV and vis,

230 respectively), see Fig. A1. (3) The long UV scans show a reduced multiplicative bias relative to the NAPS surface VMRs compared to the long scans retrieved in the visible window (zero-intercept slopes of 0.94 and 0.82 for UV and vis, respectively, see Fig. A2). This is likely due to the fact that scans in the visible window cover a greater horizontal region than in the UV (Ortega et al., 2015), and so UV scans may better capture the NO_2 field localized to the in situ instrument inlet. Therefore, only HeiPro retrievals with long UV scans have been used in this study for the comparisons with TROPOMI and Pandora-DS

235 tropospheric columns, GEM-MACH partial columns, and NAPS in situ surface NO_2.

Lastly, retrievals in which both the NO_2 profiles and aerosol extinction profiles had DOFS < 1 were excluded from the analysis to ensure that profile information was not mostly coming from the a priori NO_2 profile. In addition to providing

NO_2 profiles from 0–4 km, HeiPro also provides an integrated value from 0–4 km, thereby providing a partial NO_2 column for
240 the lower troposphere. All HeiPro data products presented here are hourly averages. From here on, surface NO_2 as well as 0–
4 km partial columns and profiles retrieved from Pandora MAX-DOAS measurements using HeiPro will be described as
HeiPro data products.

2.3 Models

2.3.1 Pratmo

245 Pratmo is a photochemical box model with detailed stratospheric chemistry that is of relevance to NO_2 (McLinden et
al., 2000; Brohede et al., 2008; Lindenmaier et al., 2011). Because the Pandora-DS observations provide NO_2 total columns
and we are interested in only the tropospheric portion, the stratospheric column must be removed. However, sun-synchronous
satellite observations of stratospheric NO_2 cannot solely be used to do this because they provide a single observation per day
whereas stratospheric NO_2 exhibits diurnal variability and Pandora measures throughout the day. Therefore, Pratmo provides
250 a modelled ratio of stratospheric NO_2 at the Pandora measurement time and the OMI overpass time. The measured OMI
stratospheric columns can then be multiplied by this modelled ratio to obtain stratospheric NO_2 columns at Pandora
measurement times. The OMI stratospheric NO_2 measurements used in this study are from version 3.0 level 2 (SPv3.0, Krotkov
et al., 2017) of NASA's standard product (SP).

2.3.2 ERA5

255 Various data products from the European Centre for Medium-Range Weather Forecasts (ECMWF) Reanalysis v5
(ERA5) were utilized in this work (Hersbach et al., 2023). As previously mentioned, pressure and temperature profiles were
used as a priori information in the HeiPro algorithm that retrieves NO_2 profiles from Pandora MAX-DOAS spectra. ERA5
pressure and temperature data from 0.1–30 km at the grid box nearest to the Downsview site were averaged at timestamps of
11:00, 14:00, 17:00, 20:00, and 23:00 UTC to produce daily a priori temperature and pressure profiles. Secondly, hourly ERA5
260 2 m temperature and surface pressure data at the grid box nearest to the Downsview site were used to calculate a 15 m NO_2
column (see Section 3 and Equation 1) to account for the rooftop location of the Pandora instrument. Additionally, planetary
boundary layer (PBL) height was obtained from ERA5 at the Downsview site to investigate how the bias among datasets varies
as a function of PBL height.

2.3.3 GEM-MACH

265 GEM-MACH is ECCC's operational regional air quality model, which provides predictions of pollutants over North
America at ~10 km horizontal resolution on an hourly timescale for a 72 h period, and is run twice per day at 0 and 12 UTC
(Moran et al., 2009; Pavlovic et al., 2016; Pendlebury et al., 2018). The model provides output for 80 vertical levels from the
surface to approximately 0.1 hPa. In this work, NO_2 profiles and partial columns from ~0–5.0 km within the model grid box

nearest to the Pandora measurement site were extracted from 2018 to 2020, with a 200 m vertical grid. GEM-MACH utilizes
270 emissions generated from inventories from the United States Environmental Protection Agency Air Emissions Modeling
Platform, from Canada's Air Pollutant Emission Inventory, and from Mexico's National Emissions Inventory. The model
includes physical and chemical processes such as tropospheric gas- and aqueous-phase chemistry, inorganic heterogeneous
chemistry, and wet and dry deposition. It should be noted that the operational version of GEM-MACH does not currently
include NO_x sources in the free troposphere, such as lightning and aircraft emissions.

275 **3 HeiPro Partial Column Comparisons**

In this section, we compare the HeiPro partial columns of NO_2 to (i) Pandora-DS tropospheric columns, (ii)
TROPOMI tropospheric columns, and (iii) GEM-MACH partial columns. It is important to note that the comparisons are not
entirely equivalent because HeiPro provides an integrated partial column from 0–4 km while TROPOMI and Pandora-DS
provide tropospheric columns and GEM-MACH provides 0–5 km partial columns. Figure 3 displays the following scatter
280 plots: HeiPro partial columns versus (a) Pandora-DS tropospheric columns, (b) TROPOMI tropospheric columns, and (c)
GEM-MACH partial columns. Three types of linear regressions are presented in Fig. 3: the first is the York linear fit (York et
al., 2004) in which the uncertainties in both datasets are incorporated into the regression, the second is the zero-intercept linear
regression, and the third is the ordinary least squares linear regression (used only for the HeiPro vs. GEM-MACH regression).
The multiplicative bias is obtained from the zero-intercept slope, and is presented as a deviation, in %, from a zero-intercept
285 slope of 1 ($100 \cdot$ (zero-intercept slope-1)). The mean relative bias is ($100 \cdot$ (HeiPro$-X$)$/X$), where X is Pandora-DS,
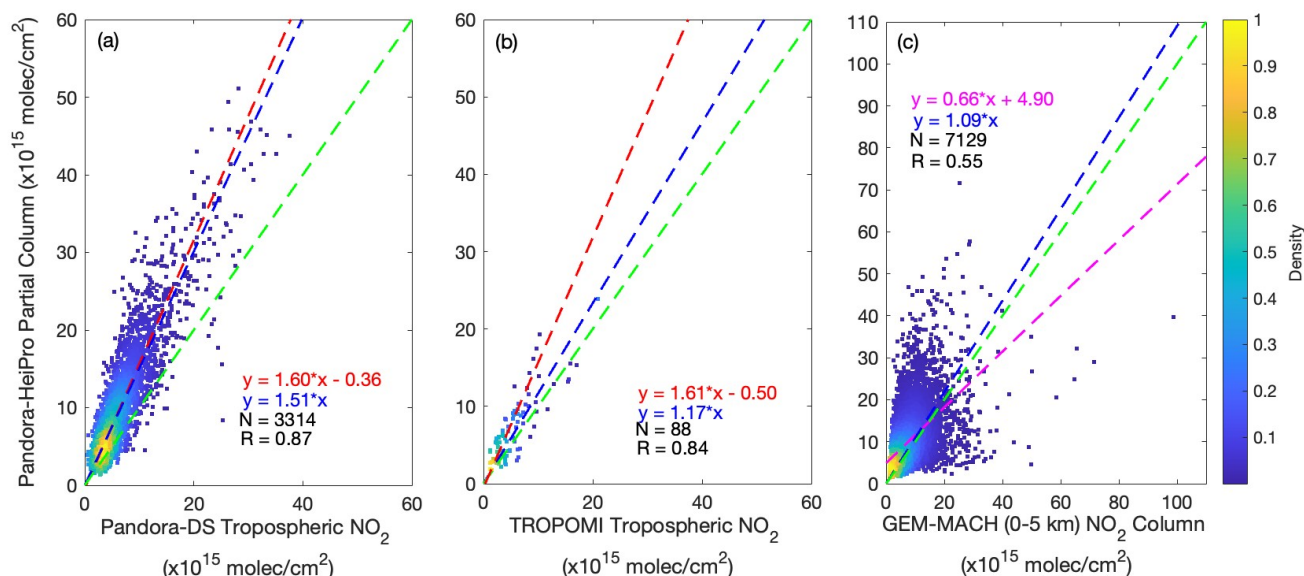TROPOMI, or GEM-MACH.

3.1 HeiPro vs. Pandora-DS

Figure 3a shows the correlation between the HeiPro partial columns and Pandora-DS tropospheric columns. This
comparison provides a good opportunity to study the differences between scattered sunlight and direct-Sun measurements by
290 the same instrument. We find that HeiPro partial columns, although measuring a smaller altitude range, are larger than Pandora-
DS tropospheric columns, with a multiplicative bias of 51% $\pm$ 0.77% and a mean relative bias of 61% $\pm$ 9.7%. Additionally,
the three-year Pandora dataset presented here provides an opportunity to investigate seasonal differences between HeiPro and
Pandora-DS. Monthly and hourly box-and-whisker plots are displayed in Fig. 4a and b, respectively. The top and bottom of
each box represent the 75th and 25th percentiles, respectively, the horizontal line within is the median value, and the whiskers
295 are the most extreme non-outlier data points, where outliers are values that are 1.5 times greater or less than the interquartile
range. The mean relative bias between the datasets for each month of the year or hour of the day are depicted by the circled
markers. Both HeiPro partial and Pandora-DS tropospheric column median values display typical seasonal and diurnal trends
for tropospheric NO_2, whereby NO_2 is greater during the winter months and morning hours from 6–9 a.m. LT due to various
chemical and dynamical factors such as increased emissions, shallow PBL, and photochemistry. The HeiPro partial columns
300 have even larger seasonal and diurnal trends compared to Pandora-DS tropospheric columns. This is further exemplified by

Atmospheric
Measurement
Techniques
Discussions

the mean relative bias between the datasets, which exhibits a strong seasonal variability, with the largest values observed in the winter (84–114%) and some of the smallest values observed in the summer (39–51%). The larger relative bias during the winter months is also shown by a larger zero-intercept slope value during the winter (1.60 ± 0.02) compared to summer (1.38 ± 0.02), as well as a greater York linear fit intercept value during the winter (2.17×10^{15} molec cm^{-2}) compared to summer

305 (0.38×10^{15} molec cm^{-2}). The mean relative bias between the two datasets is also larger from 6–9 a.m. LT (77–131%) compared to 4–7 p.m. LT (32–51%).

Figure 3: Comparisons between HeiPro (0–4 km) NO₂ partial columns (2018–2020) vs. (a) Pandora-DS tropospheric columns, (b) TROPOMI tropospheric columns, and (c) GEM-MACH (0–5 km) partial columns. The York linear

310 **regression (dashed red line), zero-intercept linear regression (dashed blue line), ordinary least squares regression (dashed magenta line), and the 1:1 line (dashed green line) are depicted. The color bar indicates the normalized density of the data points.**

Next we explore various contributing factors to the generally large bias of HeiPro to Pandora-DS. We investigate how the PBL

315 height contributes to the bias because the Pandora-DS measurements are missing the first ~15 m of the vertical column due to the rooftop instrument location while the HeiPro measurements attempt to include the first 15 m since the multi-axis viewing geometry has some sensitivity to lower layers and the HeiPro algorithm extrapolates the profile to ground level. This difference in detection may further be amplified by shallow PBL heights during winter months and morning hours, since shallower PBL heights correspond to NO₂ accumulating near the surface, which the Pandora-DS measurements do not capture. We

320 additionally investigate the effects of the SAA on the bias due to the spatiotemporal heterogeneity of NO₂ as well as the varying airmasses measured by the multi-axis and direct-Sun viewing geometries. Lastly, since NO₂ emissions increase during the winter due to increased anthropogenic emissions and shallower PBL heights, it is possible that increased emissions can

Atmospheric
Measurement
Techniques
Open Access
EGU
Discussions

contribute to the bias if there are more NO₂ emissions coming from the multi-axis azimuth viewing direction of 255° compared to the various direct-Sun viewing angles.
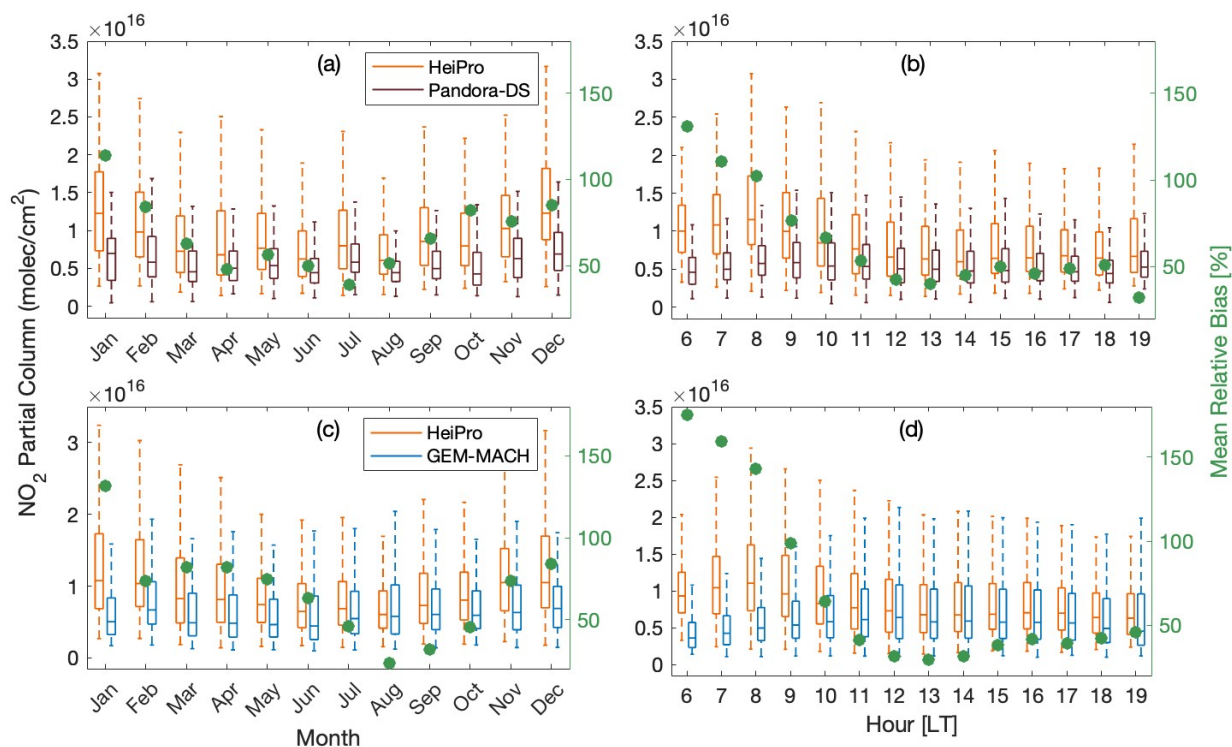
Figure 4: (a) Monthly and (b) hourly box-and-whisker plots of HeiPro 0–4 km (orange) and Pandora-DS tropospheric (brown) NO₂ columns as well as the mean relative bias between the two (green circles). (c) Monthly and (d) hourly box-and-whisker plots of HeiPro 0–4 km (orange) and GEM-MACH 0–5 km (blue) NO₂ columns as well as mean relative bias between the two (green circles). The top and bottom of each box represent the 75th and 25th percentiles, respectively, the horizontal line within is the median value, and the whiskers are the most extreme non-outlier data points, where outliers are values that are 1.5 times greater or less than the interquartile range.

The impact of the above factors on the bias is illustrated in Fig. 5a and b, which shows the zero-intercept slope, i.e., multiplicative bias, and mean relative bias, respectively, for HeiPro partial versus Pandora-DS tropospheric NO₂ columns under the following scenarios versus the SAA range, with 20° bins per SAA range: (1) HeiPro partial vs. Pandora-DS standard tropospheric NO₂ columns, (2) HeiPro partial vs. Pandora-DS 'modified' tropospheric NO₂ columns, whereby a 0–15 m column is added to the Pandora-DS column, see Section 3.1.1 for further details, (3) HeiPro partial vs. Pandora-DS modified tropospheric NO₂ columns during summer and winter, (4) HeiPro partial vs. Pandora-DS standard tropospheric NO₂ during winter only. In Sections 3.1.1–3.2.2, we quantify the contributions to the multiplicative and mean relative biases (see markers in Fig. 5c and d, respectively) between HeiPro and Pandora-DS NO₂ from various factors and indicate the scenarios that lead

Atmospheric
Measurement
Techniques
Discussions
Open Access
EGU

to the best and worst agreement between the two at this site. The relative contribution is calculated as the absolute value of the percent change in the bias after incorporating a factor (e.g., the PBL contribution is calculated as: $100 \cdot (\mid$ bias of HeiPro vs. Pandora-DS modified − bias of HeiPro vs. Pandora-DS standard$\mid$)/ bias of HeiPro vs. Pandora-DS standard, at constant SAA range), and so any decreases in the bias when incorporating a factor such as PBL are reported as positive numbers and therefore

345   as contributions to the bias.
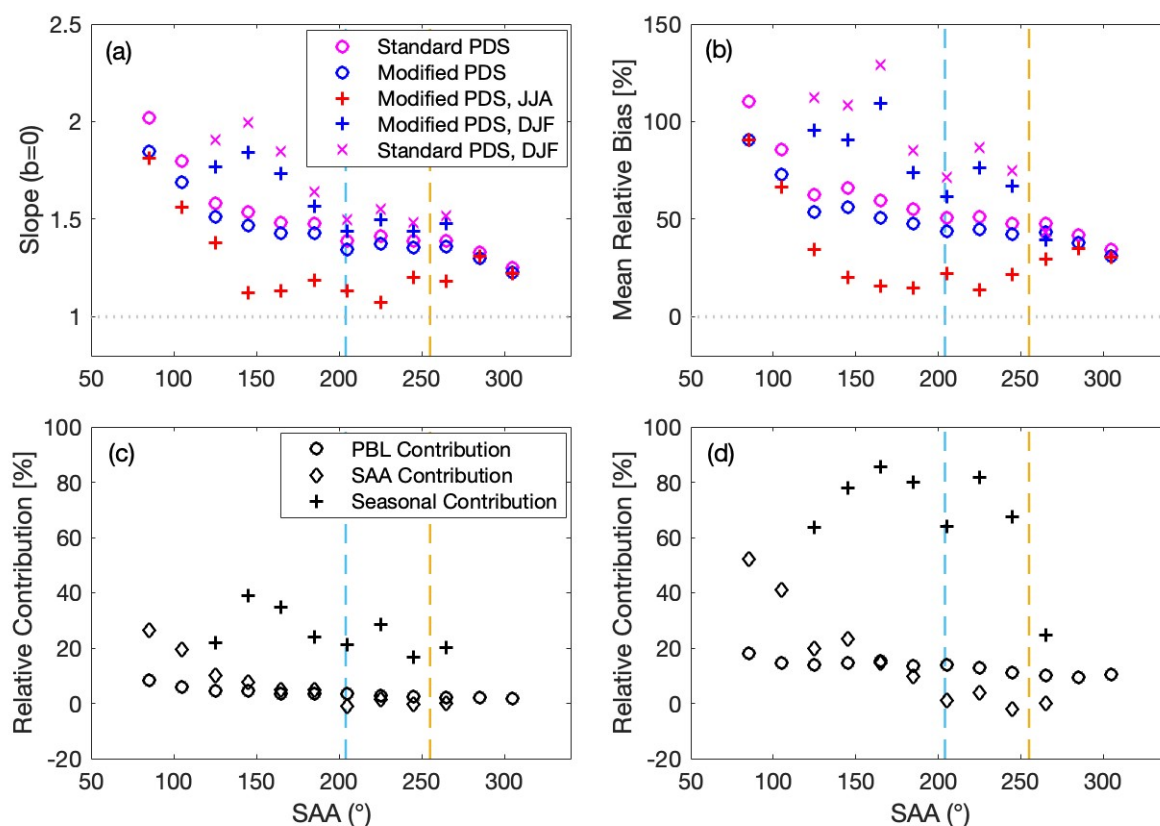
Figure 5: (a) Zero-intercept slope and (b) mean relative bias for HeiPro partial vs. Pandora-DS (PDS) tropospheric NO₂ columns under various scenarios (see legend), with relative contributions (%) from various factors (see legend) to the (c) zero-intercept slope and (d) mean relative bias. The dashed yellow lines represent the Pandora azimuth

350   **viewing angle of 255° and the dashed blue lines represent the mean SAA during the TROPOMI overpass time of 204°. Each marker represents a 20° bin of SAA, with a range of values that precede and include the marker value.**

3.1.1 PBL Height Effects

The effect of the missing 0–15 m in the Pandora-DS tropospheric column can be enhanced when the PBL height is shallow. Overall, we found that this partially contributed to why the HeiPro partial NO$_2$ columns were larger than the Pandora-

355   DS tropospheric columns but was not able to fully account for the biases observed. This was investigated by producing an

approximate 0–15 m column, which was calculated using the NAPS in situ surface NO₂ value taken as an indication of the first 15 m of the NO₂ profile at the measurement location, calculated as:

$$0 - 15m \, column = \frac{h \times VMR \times n_A \times P}{R \times T \times 10^9 \, molec. \, air} \qquad Equation \; (1)$$

360

where h is the height of the column (15 m), VMR is the volume mixing ratio of NO₂ in ppbv ($\frac{X \, molecules \, of \, NO_2}{10^9 \, molecules \, of \, air}$), n_A is Avogadro's number, P is the surface pressure in atm, R is the ideal gas constant ($8.21 \times 10^{-5} m^3 \cdot atm \cdot K^{-1} \cdot mol^{-1}$), and T is the surface temperature in K. Surface pressure and temperature values were obtained from ERA5 reanalysis data for each hour corresponding to the in situ measurement of NO₂ VMR. This column was then added to the Pandora-DS tropospheric

365 column to create a 'modified' column and the biases between HeiPro and Pandora-DS were re-examined using the modified column. The effects of the missing 15 m and the PBL height on the bias can be quantified by looking at how the multiplicative bias and mean relative bias change from the HeiPro partial versus Pandora-DS standard tropospheric columns to the HeiPro partial versus Pandora-DS modified tropospheric columns. The most notable reductions in the biases are seen when the SAA range is 66°–85°, although large multiplicative biases and mean relative differences of $> 50\%$ remain at this SAA range. Such

370 reductions in the multiplicative and relative biases (HeiPro partial column vs. Pandora-DS tropospheric column − HeiPro partial column vs. Pandora-DS modified tropospheric column) are depicted by the circles in Fig. 5c and d and termed the "PBL contribution", respectively. The largest reductions of 8.4% in the multiplicative bias and 18% in the mean relative bias occur at the SAA range of 66°–85°, which corresponds to the morning hours of 6–8 a.m. LT. This is unsurprising since the PBL height is shallow during this time, which presents a greater opportunity for any NO₂ accumulating in the first 15 m to be missed

375 by the Pandora-DS measurements. The impact of accounting for the missing 15 m then drops to negligible amounts throughout the day as the SAA increases, presumably due to a more well-mixed PBL.

3.1.2 NO₂ Heterogeneity Contribution

Another potential factor contributing to the large bias of HeiPro to Pandora-DS is the three-dimensional heterogeneity of the NO₂ field combined with the fact that multi-axis and direct-Sun viewing geometries inherently measure different

380 airmasses. Importantly, the direct-Sun and multi-axis viewing geometries point to different azimuth angles, with direct-Sun tracking the Sun and multi-axis constantly pointing to 255°, which also contributes to differences in the airmasses being probed due to the spatial heterogeneity of NO₂. To investigate how differences in viewing angles contributes to the bias, the zero-intercept slope and mean relative bias between HeiPro partial NO₂ columns versus Pandora-DS modified tropospheric NO₂ columns at each SAA range were compared to the bias at 246°–265°, i.e., Pandora-DS measurements within $\pm 10°$ of the MAX-

385 DOAS HeiPro measurements. This bias difference is represented by the diamond markers in Fig. 5c and d and termed the

14

"SAA contribution". The SAA contribution was not calculated for the SAA ranges of 266°–285° since the HeiPro bias relative to Pandora-DS in these ranges is smaller than the bias at the reference SAA range of 246°–265°.

The largest zero-intercept slope and mean relative biases (1.85 and 91%, respectively) are seen when the direct-Sun and multi-axis viewing angles are farthest apart during the measurement day in the hours from 6–8 a.m. LT. The zero-intercept slope then drops from 1.85 at the 66°–85° SAA range to 1.36 at the 246°–265° SAA range, while the mean relative bias drops from 91% to 44% for these ranges, representing 27% and 52% reductions in the multiplicative and mean relative biases, respectively. These large contributions are during the morning hours when the direct-Sun and multi-axis viewing geometries are farther apart, and the SAA contribution to the bias decreases to negligible values as the SAA increases. It is important to note that even when Pandora-DS measurements are within $\pm 10°$ of the HeiPro measurements, the biases are still large, with a zero-intercept slope of 1.30 and mean relative bias of 44%. One contribution to this bias may be the 10° differences between direct-Sun and multi-axis viewing angles, which may still exhibit NO_2 heterogeneity, as well as the different horizontal sensitivities between the direct-Sun and multi-axis viewing geometries.

Additionally, since the mean relative bias between HeiPro partial versus Pandora-DS tropospheric columns was at a maximum during winter months and minimum during summer months (see Fig. 4a), seasonal effects on the bias were investigated. The zero-intercept slope and mean relative bias between HeiPro partial versus Pandora-DS modified tropospheric columns were plotted against the SAA range for summer months (JJA) and winter months (DJF, see Fig. 5a and b), and are both larger during the winter months compared to summer months across all SAA ranges, which is consistent with the mean relative bias shown in Fig. 4a. The differences in the biases of HeiPro partial versus Pandora-DS tropospheric columns between winter and summer at each SAA range are depicted by the crosses in Fig. 5c and d and termed the "seasonal contribution". Since there are no Pandora wintertime measurements for the first two SAA ranges and the last SAA range, seasonal contributions cannot be assessed for those hours of the day (at 6 a.m. and onwards from 6 p.m., LT). The seasonal contribution to (i) the zero-intercept slope ranges from 16% to 39% and to (ii) the mean relative bias ranges from 25% to 85%, depending on the SAA range. The seasonal contribution peaks when the SAA range is between 126°–165°, and then decreases as the SAA increases. Due to increased NO_2 emissions during the winter, it is possible that the seasonal contribution stems from increased emissions from the multi-axis azimuth viewing direction of 255°, and so HeiPro measurements, and subsequently the biases towards Pandora-DS, are even larger during winter months.

Next, we investigate the spatiotemporal NO_2 heterogeneity around Downsview and assess whether we can observe the heterogeneity that supports the biases observed (i.e., large differences in the NO_2 columns between the azimuth viewing angle and the various SAAs, and even larger differences between the two from 6–9 a.m. LT and winter months). To do this, the NO_2 field around Downsview was explored using two datasets from 2018–2020: (i) TROPOMI tropospheric NO_2 columns and (ii) GEM-MACH (0–5 km) NO_2 columns. The TROPOMI pixel-averaged (Fioletov et al., 2011; Sun et al., 2018) NO_2

Atmospheric
Measurement
Techniques
Discussions
EGU
Open Access

420   field was used to investigate the larger bias in winter, while the mean GEM-MACH NO_2 field was used to investigate the larger bias in the early morning hours since TROPOMI only provides data at 13:30 LST. We found that using such datasets to demonstrate that there was NO_2 heterogeneity between the multi-axis and direct-Sun viewing directions was insufficient because (i) TROPOMI tends to underestimate NO_2 in polluted regions and is not as suited to capture small local NO_2 enhancements as MAX-DOAS measurements are (Verhoelst et al., 2021, see Section 3.2 for further discussion), and (ii) the

425   GEM-MACH model resolution of 10 km × 10 km may also not capture local enhancements and it is difficult to use model inventories as an interpretation of actual conditions since the model utilizes inventories from the year 2013. See Fig. A3 and A4 in the Appendix for the TROPOMI and GEM-MACH NO_2 fields, respectively, and for further discussion.

To summarize, the smallest biases in the dataset are observed during the summer months, when using Pandora-DS

430   modified tropospheric columns and when the SAA > 125°, which exhibit multiplicative biases of 7.2% ± 3.4% to 31% ± 2.0% and mean relative biases of 14% ± 9.0% to 35% ± 11%. We term these combined conditions the "best-case scenario", which constitutes the following: a well-mixed PBL, accounting for the missing 15 m, smaller viewing angle differences, and summer months with less NO_2 emissions. Therefore, when conditions are suitable for agreement, HeiPro partial columns show good agreement with Pandora-DS tropospheric NO_2 columns. Conversely, the largest biases are observed when using Pandora-

435   DS standard columns (i) during the winter months throughout the measurement day (see HeiPro partial column bias to Pandora-DS standard columns in Fig. 5a and b), which exhibit multiplicative and mean relative biases mostly greater than 50% and 70%, respectively, and (ii) during the early morning hours across all seasons (see HeiPro partial column bias to Pandora-DS standard columns when the SAA ≤ 105° in Fig. 5a and b), which exhibit multiplicative biases of 80% ± 2.6% to 102% ± 3.1% and mean relative biases of 86% ± 10% to 110% ± 12%. We term the conditions outlined in (i) and (ii) as the "worst-

440   case scenario". Therefore, some portion of the large bias of HeiPro to Pandora-DS may be explained by the following environmental conditions: shallow PBL, the missing 15 m in the Pandora-DS measurements, larger viewing angle differences, and increased NO_2 heterogeneity during the winter. Scatter plots for the best-case (multiplicative bias: 19% ± 1.3%; mean relative bias: 24% ± 9.7%) and worst-case (multiplicative bias: 72% ± 1.7%; mean relative bias: 101% ± 9.4%) subsets of the data are presented in Fig. A5a and b, respectively. Although the biases are minimized in the best-case scenario, nonzero

445   biases remain. This is shown in Fig. 5a and b by the offset from the dotted grey line of the HeiPro partial column bias towards Pandora-DS modified tropospheric columns during the summer months when the SAA > 125°). Possible contributing factors to the remaining bias are discussed in Section 5.

3.2 HeiPro vs. TROPOMI

Figure 3b shows the scatter plot for HeiPro partial versus TROPOMI tropospheric NO_2 columns, with HeiPro

450   exhibiting multiplicative and mean relative biases of 17% ± 4.0% and 41% ± 47%, respectively, compared to TROPOMI measurements. The relatively large uncertainty in the mean relative bias can be attributed to the larger retrieval errors in the TROPOMI tropospheric NO_2 measurements. Our findings regarding the differences between HeiPro and TROPOMI are in

accordance with a study by Verhoelst et al. (2021), who categorized the TROPOMI bias relative to ground-based MAX-DOAS
NO$_2$ into the following regimes: (1) regions with low pollution levels can have median relative differences (100 ·
455 (TROPOMI−MAX-DOAS)/MAX-DOAS) of up to −27%, (2) regions with moderate pollution levels exhibit biases between
−15% to −56%, and (3) for extremely polluted regions, differences of −37% to −74% are seen. The pollution level categories
were based on the median MAX-DOAS ground-based tropospheric columns. As Toronto is a moderately polluted region with
a median HeiPro 0–4 km partial column of 7.71×10^{15} molec cm^{-2}, our findings are in accordance with the bias range in the
moderately polluted categorization of Verhoelst et al. (2021), i.e., the median bias (TROPOMI−HeiPro) within this dataset is
460 −1.4 ×10^{15} molec cm^{-2}, with a median relative bias of −27%, as per the equation used in the study. Factors contributing to
the discrepancy between TROPOMI and MAX-DOAS NO$_2$, and therefore also the limitations of using the TROPOMI NO$_2$
field to address the HeiPro overestimation of Pandora-DS, are discussed next.

Firstly, MAX-DOAS measurements can capture more local enhancements in NO$_2$, while the satellite retrievals
465 provide a smoothed pixel representation. For example, satellite underestimation of MAX-DOAS measurements can occur if
the footprint of the emission source is smaller than the satellite footprint of 3.5 km × 5.5 km for TROPOMI (3.5 km × 7.5 km
prior to August 2019, Verhoelst et al., 2021). Additionally, the TROPOMI retrieval algorithm is sensitive to the a priori NO$_2$
profile shape, and the use of low-resolution a priori NO$_2$ profiles in the TROPOMI retrieval algorithm can contribute to the
underestimation of ground-based MAX-DOAS measurements, as shown in various studies (Zhao et al., 2020; Dimitropoulou
470 et al., 2020). For example, Zhao et al. (2020) showed a 10% reduction in the bias between TROPOMI and Pandora-DS NO$_2$
total columns when replacing the standard a priori profile in the TROPOMI retrieval algorithm with GEM-MACH, a profile
from a high-resolution regional air quality forecast model.

The TROPOMI overpass time of 13:30 LST occurs at a time of day such that the HeiPro biases relative to Pandora-
475 DS are at the lower end of the bias range (see where markers intersect with the dashed line at 204° in Fig. 5a and b). It would
be interesting to observe how the bias of geostationary NO$_2$ measurements (e.g., TEMPO) relative to ground-based direct-Sun
and multi-axis measurements changes throughout the day, given the large seasonal and diurnal dependency of the HeiPro bias
relative to Pandora-DS. The results of the HeiPro comparisons to Pandora-DS in this study can therefore aid in future ground-
based direct-Sun and MAX-DOAS validation studies of TEMPO by providing possible explanations for differences in the bias
480 between TEMPO versus MAX-DOAS and TEMPO versus direct-Sun at this measurement site.

3.3 HeiPro vs. GEM-MACH

Here we compare the HeiPro NO$_2$ partial columns to GEM-MACH. Figure 3c shows the regression between HeiPro
(0–4 km) and GEM-MACH (0–5 km) partial columns. HeiPro is greater than GEM-MACH with a multiplicative bias of 9.0%
485 ± 0.84% and a mean relative bias of 61% ± 7.5%. Figure 4c and d display monthly and hourly, respectively, box-and-whisker

plots of both datasets as well as the mean relative bias between them. As with comparisons of HeiPro to Pandora-DS, the HeiPro dataset exhibits a stronger annual cycle than GEM-MACH, with a larger interquartile range and whiskers during the winter months. The seasonal trend appears weaker in the GEM-MACH box-and-whisker plots, which do not seem to capture the seasonal pattern in NO_2. Such differences in seasonal patterns between GEM-MACH and HeiPro are further reflected in

490   the monthly mean relative biases (see circled markers), in which the winter months exhibit some of the largest percent differences (74–132%) compared to the summer months (23–63%). Also similar to the HeiPro and Pandora-DS hourly comparisons, the HeiPro versus GEM-MACH hourly comparisons exhibit the largest (99–175%) mean relative biases during the morning hours (6–9 a.m. LT), with values generally decreasing throughout the day. The large bias of HeiPro to GEM-MACH NO_2 can partially be explained by the NO_2 inventories used in the GEM-MACH model. The model inventories account

495   for surface NO_2 emissions in the PBL, but do not include lightning and aircraft emissions of NO_2 in the free troposphere. This is further demonstrated in the NO_2 profile and surface comparisons in Section 4.

Due to the similarly large biases in HeiPro partial columns relative to Pandora-DS and to GEM-MACH, as well as similar seasonal and diurnal patterns in these biases, a comparison was done between Pandora-DS and GEM-MACH (see

500   Appendix, Fig. A6). The scatter plot (Fig. A6a) shows a zero-intercept slope of 1.00 (i.e., no apparent multiplicative bias), indicating that there is good agreement between Pandora-DS tropospheric and GEM-MACH (0–5 km) partial NO_2 columns, although a positive mean relative bias ($100 \cdot$ (GEM-MACH$-$ Pandora-DS)/Pandora-DS) of 20% exists. The positive mean relative bias, indicating that GEM-MACH values are greater than Pandora-DS, is also evident in the mean monthly and hourly box-and-whisker plots in Fig. A7b and c, respectively, which show that GEM-MACH is greater than Pandora-DS, particularly

505   in the afternoon hours with an approximate mean relative bias of 30%.

4 HeiPro Surface NO_2 & Profile Comparisons

This section presents the surface NO_2 comparisons between HeiPro versus (i) NAPS in situ and (ii) GEM-MACH, as well as NO_2 profile comparisons between HeiPro and GEM-MACH. The surface comparisons are presented in Section 4.1 while the profile comparisons are presented in Section 4.2. GEM-MACH is used for the profile comparison as it is the only

510   source of NO_2 profile data available at this site. The multiplicative bias is as described in Section 3 and the mean relative bias is ($100 \cdot$ (HeiPro$-$X)/X), where X is NAPS in situ or GEM-MACH.
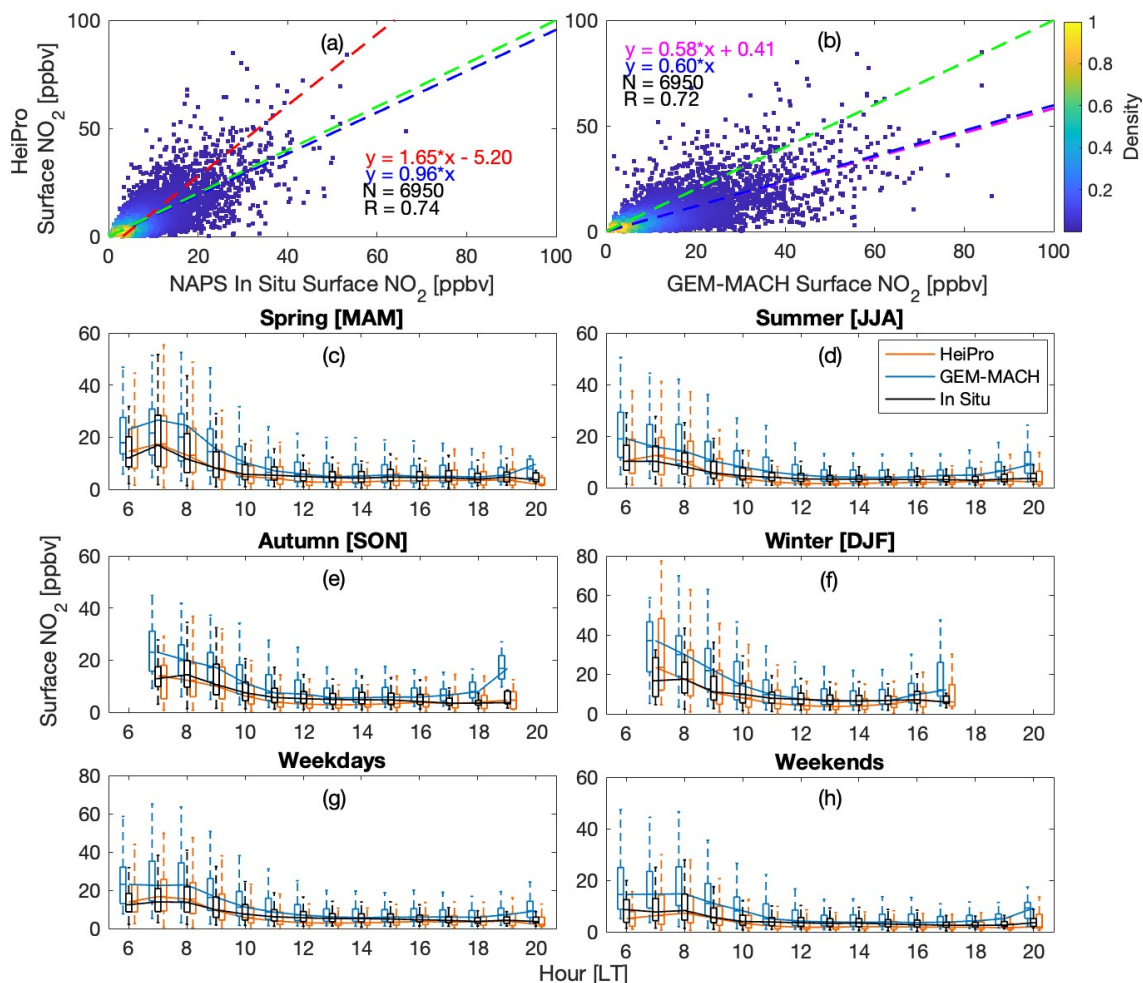
4.1 Surface NO_2 Comparisons

Figure 6 shows the scatter plots of HeiPro versus (a) NAPS in situ surface NO_2 and (b) GEM-MACH surface NO_2, whereby HeiPro surface NO_2 exhibits negative multiplicative biases of $-4.4\% \pm 0.71\%$ and $-40\% \pm 0.47\%$ to NAPS in situ

515   and GEM-MACH, respectively. Likewise, HeiPro exhibits mean relative biases of $-8.9\% \pm 7.6\%$ and $-36\% \pm 2.4\%$ to NAPS in situ and GEM-MACH, respectively. Figure 6c–f shows box-and-whisker plots of the seasonal diurnal trends of HeiPro, GEM-MACH, and NAPS in situ surface NO_2 (box-and-whisker plots are as defined in Section 3.1). All datasets

display peaks in surface NO_2 around 6–8 a.m. LT and decrease throughout the day, capturing the diurnal trend of surface NO_2, which is shaped by emission intensity, PBL dynamics, and photochemistry. Additionally, the small negative bias between

520   HeiPro and NAPS in situ is evident in the diurnal plots throughout most of the measurement day and across all seasons. On the other hand, the larger negative bias of HeiPro to GEM-MACH is evident in the diurnal plots throughout the measurement day, particularly during the morning hours.

       Across all seasons, the largest surface NO_2 values are from the GEM-MACH data from 6–9 a.m. LT. The GEM-

525   MACH surface NO_2 is likely to be overestimated due to an outdated NO_2 inventory being used in the model, which does not account for reduced NO_2 emissions over the years or reduced commutes during the COVID-19 lockdown periods in 2020 (Zhao et al., 2022). Additionally, all three datasets capture a stronger diurnal trend on weekdays (Fig. 6g) compared to the diurnal trend on weekends (Fig. 6h), which shows smaller median values as well as interquartile and whisker ranges. It is important to note that the HeiPro seasonal diurnal surface NO_2 values, as well as weekday versus weekend trends, are more

530   closely aligned to NAPS in situ surface NO_2 than GEM-MACH is to NAPS in situ surface NO_2. HeiPro provides a reasonable estimate of surface NO_2 values as well as the seasonal diurnal pattern of surface NO_2 but tends to underestimate the intensity during the evening hours. Contributions to the discrepancy between HeiPro and NAPS in situ surface NO_2 are discussed next.

Figure 6: Comparisons of surface NO₂ VMR (2018–2020) for HeiPro vs. (a) NAPS in situ, and (b) GEM-MACH. The
535   **dashed lines and color bar are as indicated in Fig. 3. (c)–(f) Seasonal diurnal and (e), (f) weekday, weekend box-and-
whisker plots of HeiPro (orange), GEM-MACH (blue), and NAPS in situ (black) surface NO₂ VMRs. Box-and
whisker values are as defined in Fig. 4.**

Due to the vertical offset of 11 m between the Pandora and in situ instruments (the former on the rooftop at 15 m and

540   the latter at 4 m above ground level) and the heterogeneity of the NO₂ field, PBL height was investigated as a potential source

of discrepancy between HeiPro and NAPS in situ surface NO₂. The relative bias of HeiPro to NAPS in situ ($100 \cdot$

(HeiPro−NAPS in situ)/NAPS in situ) versus PBL height range is presented in the box-and-whisker plots of Fig. 7. The box-

and-whisker values are as defined in Section 3.1. The PBL range were chosen to ensure that the number of data points in each

bin were in the same order of magnitude. For the shallowest PBL range from 0–0.40 km, the upper and lower extents of the

545   boxes and whiskers indicate that, at times, HeiPro is greater than NAPS in situ surface NO₂, while at other times, HeiPro is

smaller than NAPS in situ. Although the HeiPro profiles have some sensitivity to the 15 m of the atmospheric column below the instrument altitude, the vertical offset of the Pandora instrument may impact its sensitivity to those 15 m. It is not known how the HeiPro surface value would change if the instrument were on ground level or had negative elevation viewing angles (and therefore more sensitivity to the first 15 m). Nonetheless, it appears that the shallowest PBL range exhibits a larger range

550 of differences but smaller (less negative) median values (e.g., for summer, whisker range: -128% to 195%; median value: -10%) compared to the largest PBL range (e.g., for summer, whisker range: -119% to 22%; median value: -51%), and so the vertical offset between the instruments may contribute to the larger range of differences observed when the PBL height is shallow and there is more vertical NO_2 heterogeneity. In addition to the narrower whisker range for PBL heights > 0.90 km, this PBL range consistently also has median values of approximately -50% across all seasons (see horizontal lines within

555 each box in Fig. 7). At this PBL range, which corresponds to the afternoon periods when surface NO_2 is at a minimum, the airmass measured by both the Pandora and NAPS instruments is more uniform, which may contribute to a more consistent difference between the two, hence the narrower whisker range. Additionally, the NAPS instrument measures a very localized airmass due to the nature of the in situ technique, while the HeiPro measurements stem from an instrument field-of-view of $1.6°$ (Herman et al., 2009) and a photon effective path length between 5 and 10 km for UV measurements (Ortega et al., 2015).

560 These varying horizontal sensitivities between HeiPro and NAPS in situ, combined with spatiotemporal NO_2 heterogeneity, can also contribute to differences in the airmasses being measured.

Atmospheric
Measurement
Techniques
Discussions

Open Access

EGU
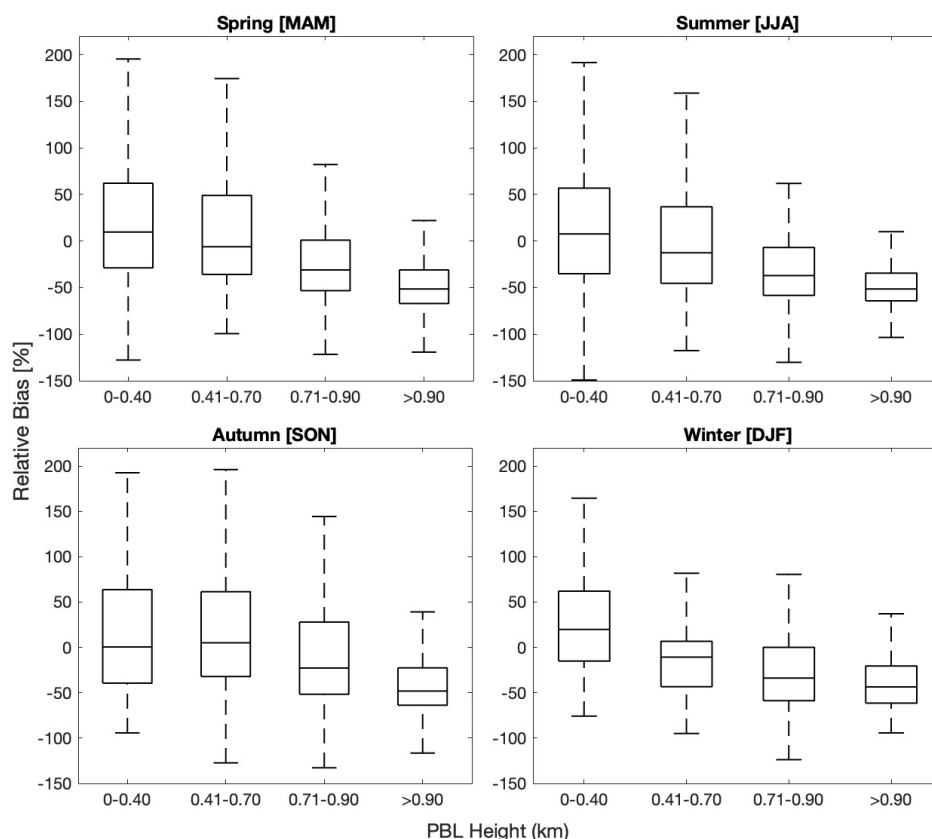
Figure 7: Seasonal box-and-whisker plots of the relative bias of HeiPro to NAPS in situ surface NO₂ vs. PBL height range. Box-and-whisker values are as defined in Fig. 4.

4.2 Profile Comparisons

Figure 8 shows the seasonal median NO₂ profiles for HeiPro, GEM-MACH, and GEM-MACH smoothed by the HeiPro averaging kernel. The shaded regions represent the 90th percentile (right of solid line) and 10th percentile (left of solid line) values for HeiPro and GEM-MACH but are not shown for GEM-MACH smoothed for visual clarity purposes. The seasonal median NAPS in situ surface NO₂ values are also displayed for reference. As stated previously, the surface values for HeiPro and GEM-MACH were extrapolated from the midpoint of the grid level closest to the surface (e.g., 0–200 m for HeiPro), for each available profile. Due to the presence of some lofted layers in the HeiPro profiles, in which the 0–200 m grid level NO₂ VMR is less than that of the 200–400 m grid level, the extrapolated surface VMR for such cases is then smaller than that of the grid level closest to the surface. When plotting the median profiles, as was done in Fig. 8, this appears to skew the profile shape (see HeiPro profiles near 0 m in Fig. 8), and it appears that the extrapolation was not linear with respect to the near-surface values, though it is the case that each profile extrapolation to the surface was linear from the grid level closest to the surface. HeiPro, NAPS in situ, and GEM-MACH datasets all have larger median surface NO₂ values during the winter

months (5.7, 7.8, and 10 ppbv, respectively) compared to spring (4.2, 5.4, and 7.7 ppbv), summer (2.7, 4.0, and 6.5 ppbv), and autumn (4.3, 5.7, and 8.1 ppbv). This is in accordance with winter conditions that increase surface NO_2 such as larger anthropogenic emissions, meteorological conditions, etc.
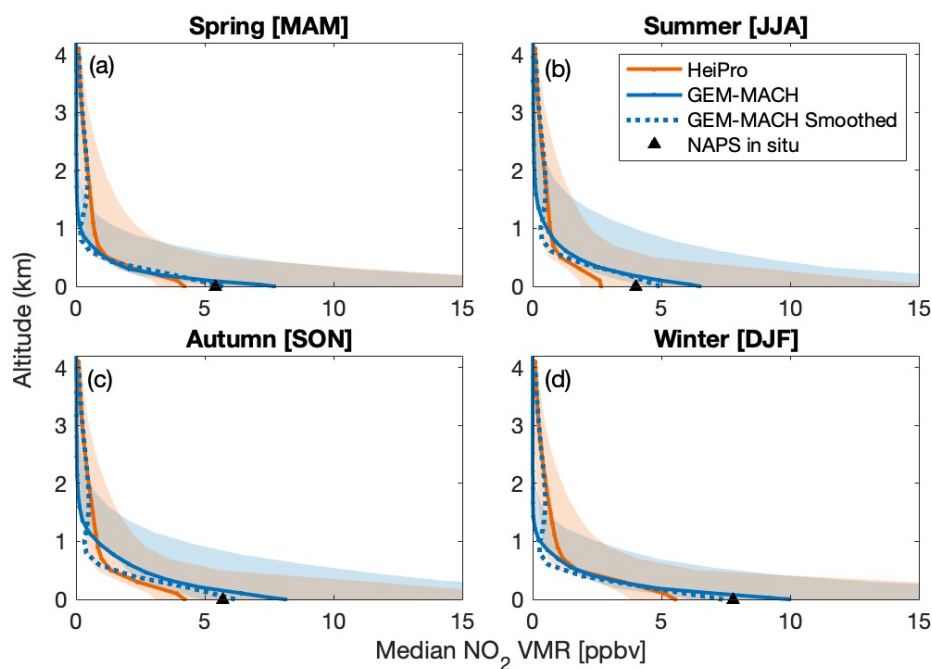
Figure 8: HeiPro (solid orange line), GEM-MACH (solid blue line), and GEM-MACH smoothed (dotted blue line) median NO_2 profiles for each season. The shaded regions represent the 90th percentile (right of line) and 10th percentile (left of line) values for HeiPro and GEM-MACH. The black triangles indicate the seasonal median NAPS in situ surface NO_2 values.

Across all seasons, the HeiPro median profiles underestimate the GEM-MACH median surface and near-surface NO_2 values from 0–0.80 km. At an altitude of approximately 0.80 km and above, the HeiPro median profiles then overestimate the GEM-MACH median profiles. As stated previously, this is likely due to the NO_2 inventories used in the GEM-MACH model, which (i) do not account for free tropospheric NO_2 sources while HeiPro measurements have some sensitivity to such layers, and (ii) utilize older inventories that do not account for reduced emissions over the years. Although it is difficult to assess the accuracy of the HeiPro NO_2 profiles without the availability of in situ NO_2 profiles at this site, it is worthwhile to note that discrepancies between HeiPro and GEM-MACH profiles can be explained by the model inventories, and that HeiPro seems to provide a conservative estimate of the NAPS in situ value at the surface, where NO_2 VMRs are typically the largest. Additionally, while the GEM-MACH surface NO_2 VMRs are appropriately larger in the winter, this trend is not similarly captured for the GEM-MACH partial columns (see box-and-whisker plots in Fig. 4c). On the other hand, both the HeiPro

surface NO_2 and partial columns display increased values during winter months. While the unsmoothed GEM-MACH profile is biased high/low near the surface/above 1 km compared to HeiPro due to the model inventory, the smoothed GEM-MACH profile shows better agreement with HeiPro as it accounts for the MAX-DOAS measurement limitations and vertical sensitivity.

5 Conclusions

This study produced a three-year dataset of NO_2 profiles and partial columns from 0–4 km at Downsview, Ontario by applying HeiPro, an optimal estimation profile retrieval algorithm, to Pandora UV MAX-DOAS measurements. The HeiPro partial NO_2 columns obtained from the profiles were found to overestimate the partial columns from Pandora-DS, TROPOMI, and GEM-MACH, with multiplicative biases of 51%, 17%, and 9.0%, respectively, and mean relative biases of 61%, 41%, and 61%, respectively. The seasonal and diurnal trends in the mean relative biases between HeiPro and Pandora-DS as well as HeiPro and GEM-MACH were similar, with larger mean relative biases during the winter months and morning hours from 6–8 a.m. LT. Additionally, HeiPro partial columns exhibit larger variability, as evidenced by the larger box-and-whisker ranges in Fig. 4a and b, compared to Pandora-DS; this is consistent with a study by Pinardi et al. (2020), who found that MAX-DOAS measurements tend to depict a fuller range of NO_2 variability due to their ability to measure under partially cloudy conditions, while direct-Sun measurements require clear skies. Although Fig. 4 presents hourly-averaged coincident measurements between HeiPro and Pandora-DS, the measurements are not perfectly coincident during that hour that is averaged, which can also contribute to the differences between the direct-Sun and MAX-DOAS datasets. Seasonal and diurnal comparisons to TROPOMI were not possible due to limited datapoints during winter months and there being one measurement per day, respectively. The TROPOMI bias to HeiPro reported in this study (−27%) matched the bias range reported by Verhoelst et al. (2021) for a moderately polluted region, and it would be interesting to investigate how this satellite bias relative to ground-based MAX-DOAS measurements changes throughout the day using a geostationary satellite data product such as that of TEMPO (Zoogman et al., 2017).

We found that the HeiPro bias relative to Pandora-DS can partially be explained by several factors, which vary in their contributions to the bias throughout the day. The PBL height, combined with the missing 0–15 m partial column in the Pandora-DS measurements, contributed a maximum of 8.4% of the multiplicative bias and 18% of the mean relative bias in the morning hours, with these values declining to < 5% in the evening hours. The differences between the direct-Sun and multi-axis azimuthal viewing angles throughout the day, combined with the spatiotemporal heterogeneity of the NO_2 field, contributed a maximum of 27% and 52% of the multiplicative and mean relative biases, respectively, when the two viewing angles were farthest apart, and declined throughout the day as the direct-Sun azimuthal viewing angle approached the multi-axis one. Lastly, the seasonal contributions to the multiplicative and mean relative biases ranged from 16–39% and 25–85% respectively, with systematically larger biases during the winter months. We were not able to assess for seasonal contributions at certain SAA ranges during the wintertime since there were no measurements during these hours, i.e., at 6 a.m. and onwards

630   from 6 p.m. LT. We utilize best-case (multiplicative bias: 19%; mean relative bias: 24%) and worst-case (multiplicative bias: 72%; mean relative bias: 101%) scenarios to exemplify how these contributing factors affect the bias, and note that when these factors are minimized, the bias decreases and the agreement between HeiPro and Pandora-DS significantly improves.

Although not quantified, there are various possible contributions and sources of uncertainty to the remaining bias. (1) The HeiPro and Pandora-DS comparisons use hourly averages and are not perfectly temporally coincident. This, combined

635   with NO_2 variability, is likely contributing to the scatter within the data. (2) The HeiPro data stems from NO_2 retrieved in the UV window (338–370 nm) while the Pandora-DS data stems from NO_2 retrieved in the 400–440 nm range, so differences in the spectroscopic analysis may be a factor. (3) Uncertainties in the Pratmo model that was used to calculate OMI stratospheric NO_2 throughout the day can overestimate or underestimate Pandora-DS tropospheric NO_2, thereby underestimating or overestimating the bias, respectively. We do not believe that the use of OMI stratospheric NO_2 itself contributed to the large

640   bias, since, for example, TROPOMI stratospheric NO_2 was greater than OMI stratospheric NO_2 at this site. (4) The AOD retrieved from HeiPro is used as a parameter for the radiative transfer model of the trace gas profile retrieval as it helps to constrain the atmospheric light path. Inaccuracies in this retrieved AOD can therefore lead to errors in the NO_2 retrievals. (5) The ERA5 temperature profile data utilized in the HeiPro algorithm may underestimate measurements, which can contribute 3% to the remaining bias (as demonstrated by a sensitivity test that was performed with HeiPro and variable temperature

645   inputs, results not shown). (6) The a priori NO_2 profile used in the retrievals may also contribute to the HeiPro bias towards Pandora-DS. Although a conservative surface VMR of ~3.5 ppbv was used for the a priori profile, it is difficult to know if the upper layers of the a priori profile are conservative estimates, given the limited in situ profile information at this site. It is possible that the VMR values in the upper layers of the a priori profile are larger than the true values, which would contribute to the larger HeiPro bias relative to Pandora-DS.

650

Additionally, we investigated whether the NO_2 heterogeneity that we believe is contributing to the HeiPro bias to Pandora-DS can be supported by TROPOMI and GEM-MACH NO_2 fields at the measurement site. Overall, we were not able to utilize these datasets to show strong NO_2 heterogeneity between the two viewing geometries during the early morning hours and during the winter months. This suggests that satellite measurements and model output may not capture small-scale NO_2

655   enhancements: TROPOMI provides a smoothed representation of the NO_2 field and lacks sensitivity to the boundary layer due to the use of low-resolution a priori profiles, while GEM-MACH may not accurately represent real-time NO_2 gradients and intensities. Pandora MAX-DOAS measurements may therefore provide a better tool for probing lower tropospheric NO_2 and its heterogeneity around a measurement site since the sensitivity and temporal coverage of satellites are limited, in situ measurements are spatially limited, and the direct-Sun measurement viewing geometry is subject to the Sun's position and

660   clear-sky conditions.

While HeiPro NO_2 partial columns are larger than Pandora-DS, GEM-MACH, and TROPOMI, HeiPro surface NO_2 agrees reasonably well with NAPS in situ, with a mean relative bias of $-8.9\% \pm 7.6\%$, and appears to underestimate GEM-MACH, with a mean relative bias of $-36\% \pm 2.4\%$. This underestimation of GEM-MACH was consistent across all measurement hours of the day and all seasons, while HeiPro more closely matched the diurnal and seasonal trends of NAPS in situ surface NO_2. In comparing the HeiPro and GEM-MACH NO_2 profiles, GEM-MACH generally overestimates HeiPro across all seasons from 0–0.80 km with a mean relative bias of 61%, but above 0.80 km, the GEM-MACH profiles decrease more steeply with altitude, and GEM-MACH underestimates HeiPro with a mean relative bias of -81%. These discrepancies as a function of altitude can be explained by the GEM-MACH model inventories. The smoothed GEM-MACH profile more closely matches the HeiPro profile across all seasons (mean relative bias from 0–0.80 km: 34%, mean relative bias above 0.80 km: -8.0%) as the measurement limitations are removed in the comparison. In summary, the three-year NO_2 profile dataset presented in this study provides information about the spatiotemporal vertical distribution of NO_2 and can be used to assess discrepancies between spaceborne and ground-based NO_2 measurements.

Appendix A
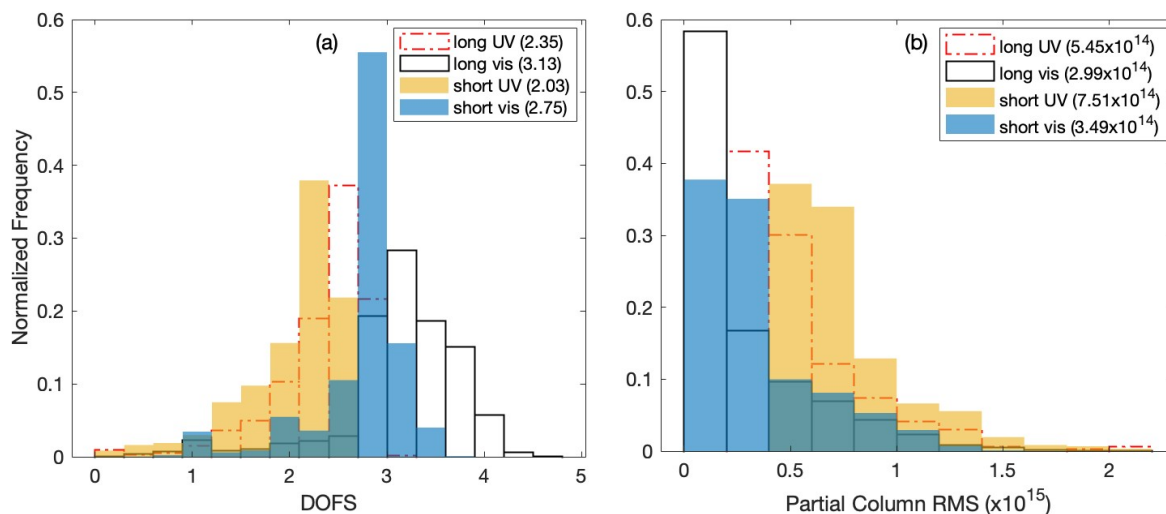
Figure A1: (a) Histogram of the normalized frequency of degrees of freedom for signal (DOFS) for the retrieved
700   **profiles from each type of Pandora multi-axis scan, where the median values are indicated in brackets. (b) Same as**
(a) but for partial column RMS fitting residuals.
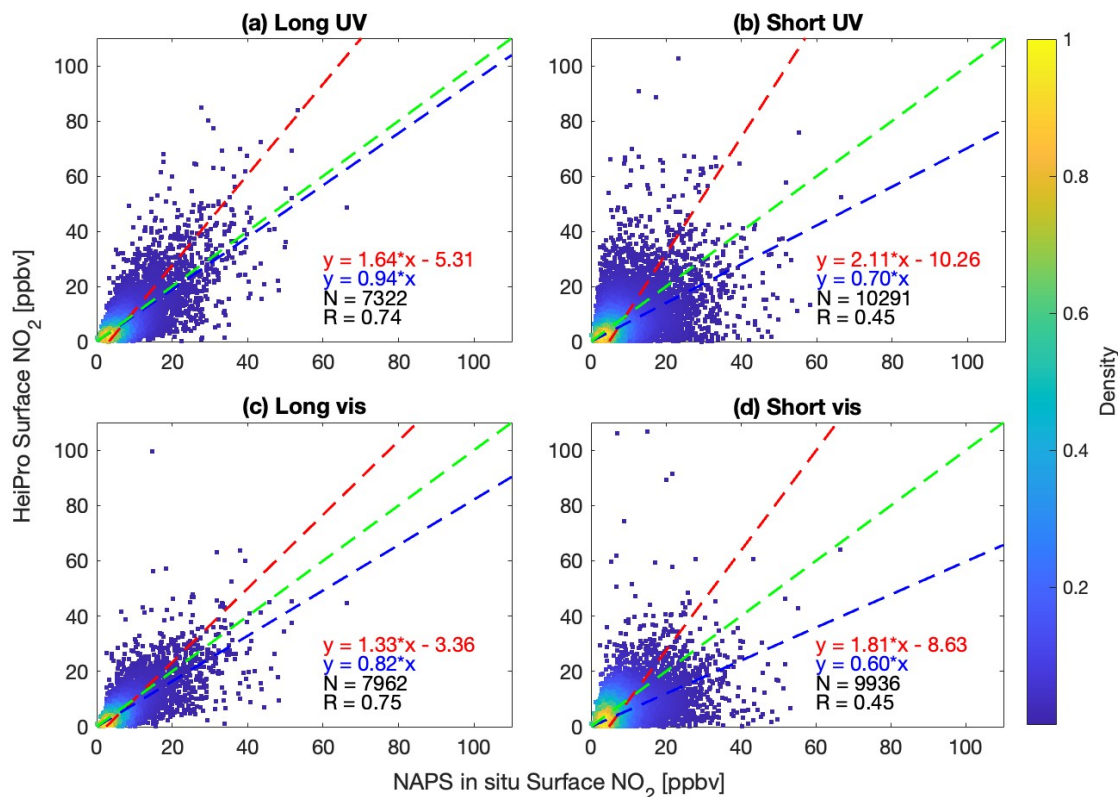
Figure A2. Scatter plots for the HeiPro surface NO₂ vs. NAPS in situ surface NO₂ VMRs for scan types and retrieval
705   windows of (a) long UV, (b) short UV, (c) long vis, and (d) short vis. Only the long UV scans were incorporated in the
results of this work. The dashed lines and color bar are as indicated in Fig. 3.

In Figs. A3 and A4, various measurement lines of sight are depicted. Figure A3a–b displays the TROPOMI pixel-
averaged NO₂ field from 2018–2020 for summer and winter months, respectively. The MAX-DOAS azimuth viewing angle
710   (255°) and direct-Sun viewing angle (average during summer or winter time periods) are shown. A marker indicates the
horizontal extent of the multi-axis path length, i.e., the effective path length. For UV MAX-DOAS measurements, this value
is in the range of 5–10 km, and so a horizontal path length of 7.5 km is indicated in the figures (Ortega et al., 2015). During
both summer and winter, there does not appear to be an obvious difference in NO₂ between the Pandora MAX-DOAS azimuth
viewing angle and the direct-Sun viewing angle at this time of day. However, there are limitations to using the TROPOMI
715   NO₂ field to investigate the HeiPro bias to Pandora-DS, since the TROPOMI data itself underestimates HeiPro and may be
insufficient to address how NO₂ heterogeneity from local emissions contributes to the HeiPro overestimation (discussed in
Section 3.2). The single temporal datapoint from TROPOMI (1:30 LST) also prevents an investigation as to how

spatiotemporal NO$_2$ heterogeneity around Downsview is impacting the HeiPro overestimation. Alternatively, the GEM-MACH dataset allows an exploration of how the NO$_2$ heterogeneity changes throughout the day and is discussed next.
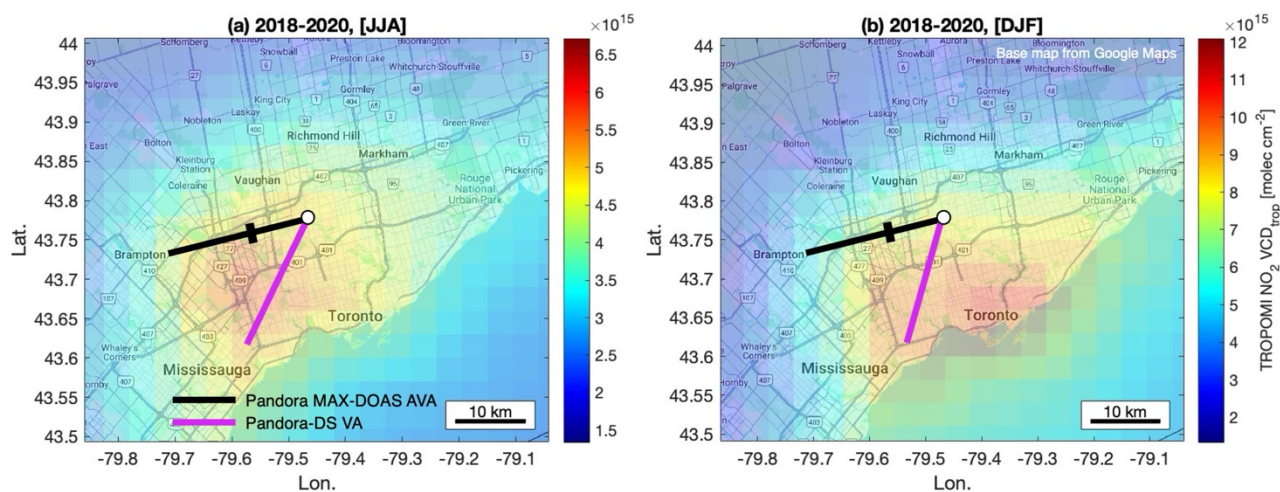

720

Figure A3. TROPOMI pixel-averaged NO$_2$ field: (a) 2018–2020, summer only; (b) 2018-2020, winter only, around Downsview (white circle), with the MAX-DOAS azimuth viewing angle depicted by the black line and the mean direct-Sun viewing angle during the TROPOMI overpass time (13:30 LT) depicted by the magenta line. The average MAX-DOAS effective path length of 7.5 km is depicted by the black marker along the line of sight.

725

In Fig. A4a–c, the 2018–2020 mean NO$_2$ field from GEM-MACH is displayed for 7 a.m., 1 p.m., and 5 p.m. LT, respectively, with the Pandora-DS viewing angles shown for each time of day. From the 7 a.m. field, it is not evident that a spatially heterogeneous NO$_2$ field, combined with differences in viewing geometries, is contributing to the larger bias of HeiPro to Pandora-DS during the early morning hours, since the direct-Sun viewing angle at this time of day faces a similarly polluted region to the multi-axis viewing direction. Although Fig. 5 shows that the bias decreases throughout the day as the sampling
730 directions approach one another, the difference in NO$_2$ levels between the two sampling directions in the GEM-MACH NO$_2$ field does not reflect that, possibly due to limitations in using model data to capture local enhancements in NO$_2$.
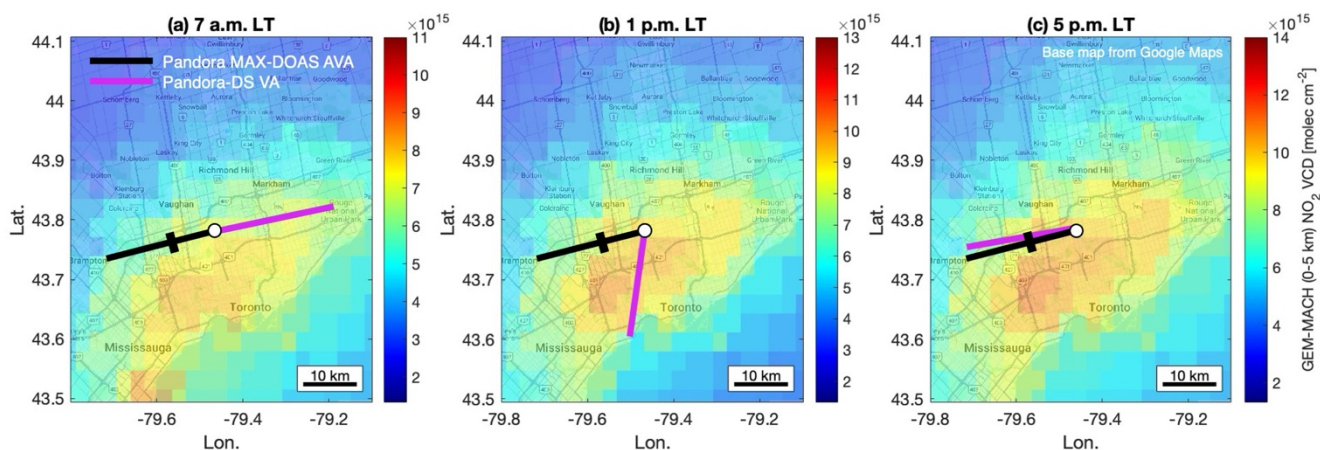
Figure A4. GEM-MACH averaged NO$_2$ field from 2018–2020 at (a) 7 a.m. LT, (b) 1 p.m. LT, and (c) 5 p.m. LT around
Downsview (white circle), with the MAX-DOAS azimuth viewing angle and average direct-Sun viewing angle during the
corresponding times depicted by the black and magenta lines, respectively. The MAX-DOAS effective path length (7.5 km)
is depicted by the black marker along the line of sight.
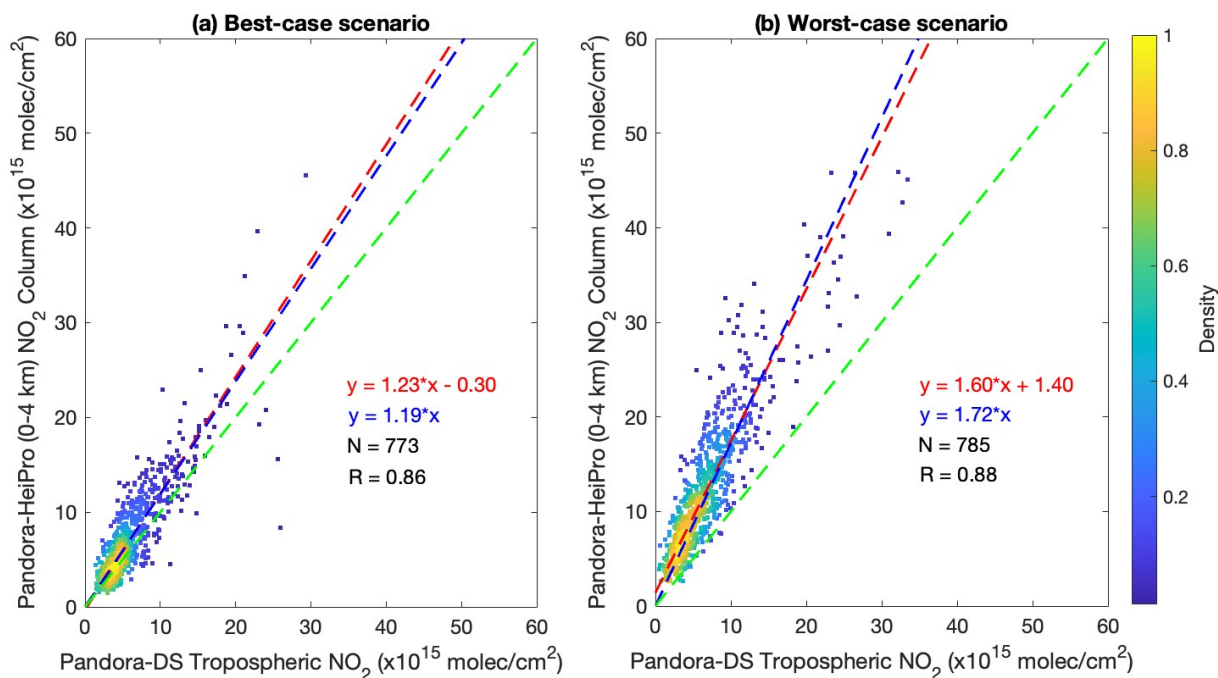
Figure A5. Scatter plots for HeiPro (0–4 km) vs. Pandora-DS tropospheric NO$_2$ columns under (a) best-case scenario
conditions (utilizing modified Pandora-DS tropospheric columns during summer months with measurements of SAA >
125°) and (b) worst-case scenario conditions (utilizing standard Pandora-DS tropospheric columns during (i) winter months
and (ii) 6–7 a.m. across remaining seasons). The dashed lines and color bar are as indicated in Fig. 3.

30
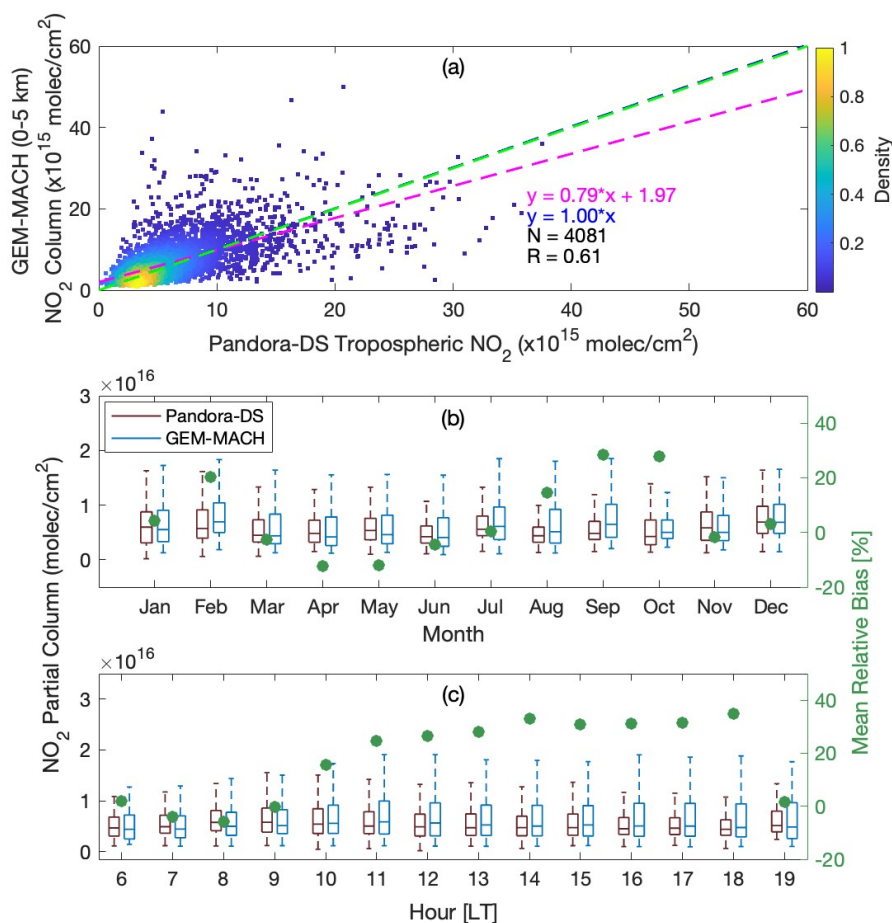
Figure A6. (a) Scatter plot for the GEM-MACH (0–5 km) vs. Pandora-DS tropospheric NO₂. The dashed lines and color bar
745   are as indicated in Fig. 3. (b) Monthly and (c) hourly box-and-whisker plots of Pandora-DS tropospheric (brown) and GEM-
MACH (0–5 km, blue) NO₂ columns as well as the mean relative bias between the two (green circles). Box-and-whisker
values are as defined in Fig. 4.

750

755

Atmospheric
Measurement
Techniques
Discussions

Data availability

Pandora data (L1 multi-axis spectra and L2 direct-Sun NO_2 total columns) are available from the Pandonia network (https://data.pandonia-global-network.org/Downsview/Pandora103s1/; Pandonia Global Network, 2024). OMI NO_2 SPv3.1

760   data are available from https://disc.gsfc.nasa.gov/ (NASA, 2020). TROPOMI L2 NO_2 data are available on the Copernicus Open Access Hub at https://scihub.copernicus.eu (ESA, 2024). The NAPS in situ data can be downloaded from https://data-donnees.az.ec.gc.ca/data/air/monitor/national-air-pollution-surveillance-naps-program/, last accessed on 10 September 2024. The HeiPro data (O_4 and NO_2 dSCDs that went into the retrievals as well as the subsequent profile retrievals) are made available at https://borealisdata.ca/dataset.xhtml?persistentId=doi:10.5683/SP3/J8PDHW.

765

Competing interests

775   At least one of the authors is a member of the editorial board of *Atmospheric Measurement Techniques*.

790

Atmospheric
Measurement
Techniques
Discussions

References

Alwarda, Ramina; Kristof Bognar; Xiaoyi Zhao; Vitali Fioletov; Jonathan Davies; Sum Chi Lee; Debora Griffin; Alexandru Lupu; Udo Frieß; Alexander Cede; Yushan Su; Kimberly Strong, 2024, "Replication Data for: Retrieval of NO_2 profiles from three years of Pandora MAX-DOAS measurements in Toronto, Canada", https://doi.org/10.5683/SP3/J8PDHW, Borealis, V1

795 Beirle, S., Platt, U., Wenig, M., and Wagner, T.: Weekly cycle of NO_2 by GOME measurements: a signature of anthropogenic sources, Atmos. Chem. Phys., 3, 2225–2232, 2003.

Blechschmidt, A.-M., Arteta, J., Coman, A., Curier, L., Eskes, H., Foret, G., Gielen, C., Hendrick, F., Marécal, V., Meleux, F., Parmentier, J., Peters, E., Pinardi, G., Piters, A. J. M., Plu, M., Richter, A., Segers, A., Sofiev, M., Valdebenito, Á. M., Van Roozendael, M., Vira, J., Vlemmix, T., and Burrows, J. P.: Comparison of tropospheric NO_2 columns from MAX-DOAS
800 retrievals and regional air quality model simulations, Atmos. Chem. Phys., 20, 2795–2823, https://doi.org/10.5194/acp-20-2795-2020, 2020.

Brohede, S., McLinden, C. A., Urban, J., Haley, C. S., Jonsson, A. I., and Murtagh, D.: Odin stratospheric proxy NO_y measurements and climatology, Atmos. Chem. Phys., 24, 2008.

Burrows, J. P., Weber, M., Buchwitz, M., Rozanov, V., Ladstätter-Weißenmayer, A., Richter, A., DeBeek, R., Hoogen, R.,
805 Bramstedt, K., Eichmann, K.-U., Eisinger, M., and Perner, D.: The Global Ozone Monitoring Experiment (GOME): Mission Concept and First Scientific Results, J. Atmos. Sci., 56, 151–175, https://doi.org/10.1175/1520-0469(1999)056<0151:TGOMEG>2.0.CO;2, 1999.

Cede, A.: Manual for Blick Software Suite 1.8, available at: https://www.pandonia-global-network.org/wp-content/uploads/2021/09/BlickSoftwareSuite_Manual_v1-8-4.pdf, last accessed: 16 April 2024.
810
Danckaert, T., Fayt, C., Roozendael, M. V., Smedt, I. D., Letocart, V., Merlaud, A., and Pinardi, G.: QDOAS Software user manual, available at: http://uv-vis.aeronomie.be/software/QDOAS/QDOAS_manual.pdf, last access: 16 April 2024.

Dimitropoulou, E., Hendrick, F., Pinardi, G., Friedrich, M. M., Merlaud, A., Tack, F., De Longueville, H., Fayt, C., Hermans,
815 C., Laffineur, Q., Fierens, F., and Van Roozendael, M.: Validation of TROPOMI tropospheric NO_2 columns using dual-scan multi-axis differential optical absorption spectroscopy (MAX-DOAS) measurements in Uccle, Brussels, Atmos. Meas. Tech., 13, 5165–5191, https://doi.org/10.5194/amt-13-5165-2020, 2020.

ECCC Canadian Environmental Sustainability Indicators: Air Quality; Environment and Climate Change Canada: Dufferin St North York, ON, Canada, 2016; ISBN 978-0-660-06016-3.
820
Fioletov, V. E., McLinden, C. A., Krotkov, N., Moran, M. D., and Yang, K.: Estimation of SO_2 emissions using OMI retrievals, Geophys. Res. Lett., 38, L21811, https://doi.org/10.1029/2011GL049402, 2011.

Frieß, U., Monks, P. S., Remedios, J. J., Rozanov, A., Sinreich, R., Wagner, T., and Platt, U.: MAX-DOAS O_4 measurements: A new technique to derive information on atmospheric aerosols: 2. Modeling studies, J. Geophys. Res., 111, D14203,
825 https://doi.org/10.1029/2005JD006618, 2006.

Frieß, U., Sihler, H., Sander, R., Pöhler, D., Yilmaz, S., and Platt, U.: The vertical distribution of BrO and aerosols in the Arctic: Measurements by active and passive differential optical absorption spectroscopy, J. Geophys. Res., 116, D00R04, https://doi.org/10.1029/2011JD015938, 2011.

Frieß, U., Beirle, S., Alvarado Bonilla, L., Bösch, T., Friedrich, M. M., Hendrick, F., Piters, A., Richter, A., van Roozendael,
830 M., Rozanov, V. V., Spinei, E., Tirpitz, J.-L., Vlemmix, T., Wagner, T., and Wang, Y.: Intercomparison of MAX-DOAS

vertical profile retrieval algorithms: studies using synthetic data, Atmos. Meas. Tech., 12, 2155–2181, https://doi.org/10.5194/amt-12-2155-2019, 2019.

van Geffen, J., Boersma, K. F., Eskes, H., Sneep, M., ter Linden, M., Zara, M., and Veefkind, J. P.: S5P TROPOMI NO_2 slant column retrieval: method, stability, uncertainties and comparisons with OMI, Atmos. Meas. Tech., 13, 1315–1335, https://doi.org/10.5194/amt-13-1315-2020, 2020.

van Geffen, J., Eskes, H., Compernolle, S., Pinardi, G., Verhoelst, T., Lambert, J.-C., Sneep, M., ter Linden, M., Ludewig, A., Boersma, K. F., and Veefkind, J. P.: Sentinel-5P TROPOMI NO_2 retrieval: impact of version v2.2 improvements and comparisons with OMI and ground-based data, Atmos. Meas. Tech., 15, 2037–2060, https://doi.org/10.5194/amt-15-2037-2022, 2022.

Griffin, D., Zhao, X., McLinden, C. A., Boersma, F., Bourassa, A., Dammers, E., Degenstein, D., Eskes, H., Fehr, L., Fioletov, V., Hayden, K., Kharol, S. K., Li, S., Makar, P., Martin, R. V., Mihele, C., Mittermeier, R. L., Krotkov, N., Sneep, M., Lamsal, L. N., Linden, M. ter, Geffen, J. van, Veefkind, P., and Wolde, M.: High-Resolution Mapping of Nitrogen Dioxide With TROPOMI: First Results and Validation Over the Canadian Oil Sands, Geophys. Res. Lett., 46, 1049–1060, https://doi.org/10.1029/2018GL081095, 2019.

Herman, J., Cede, A., Spinei, E., Mount, G., Tzortziou, M., and Abuhassan, N.: NO_2 column amounts from ground-based Pandora and MFDOAS spectrometers using the direct-sun DOAS technique: Intercomparisons and application to OMI validation, J. Geophys. Res., 114, D13307, https://doi.org/10.1029/2009JD011848, 2009.

Hersbach, H., Bell, B., Berrisford, P., Biavati, G., Horányi, A., Muñoz Sabater, J., Nicolas, J., Peubey, C., Radu, R., Rozum, I., Schepers, D., Simmons, A., Soci, C., Dee, D., Thépaut, J-N.: ERA5 hourly data on pressure levels from 1940 to present. Copernicus Climate Change Service (C3S) Climate Data Store (CDS), 10.24381/cds.bd0915c6 (Accessed on 21-Jan-2024), 2023.

Hersbach, H., Bell, B., Berrisford, P., Biavati, G., Horányi, A., Muñoz Sabater, J., Nicolas, J., Peubey, C., Radu, R., Rozum, I., Schepers, D., Simmons, A., Soci, C., Dee, D., Thépaut, J-N.: ERA5 hourly data on single levels from 1940 to present. Copernicus Climate Change Service (C3S) Climate Data Store (CDS), 10.24381/cds.adbb2d47 (Accessed on 21-Jan-2024), 2023.

Kim, J., Jeong, U., Ahn, M.-H., Kim, J. H., Park, R. J., Lee, H., Song, C. H., Choi, Y.-S., Lee, K.-H., Yoo, J.-M., Jeong, M.-J., Park, S. K., Lee, K.-M., Song, C.-K., Kim, S.-W., Kim, Y. J., Kim, S.-W., Kim, M., Go, S., Liu, X., Chance, K., Chan Miller, C., Al-Saadi, J., Veihelmann, B., Bhartia, P. K., Torres, O., Abad, G. G., Haffner, D. P., Ko, D. H., Lee, S. H., Woo, J.-H., Chong, H., Park, S. S., Nicks, D., Choi, W. J., Moon, K.-J., Cho, A., Yoon, J., Kim, S., Hong, H., Lee, K., Lee, H., Lee, S., Choi, M., Veefkind, P., Levelt, P. F., Edwards, D. P., Kang, M., Eo, M., Bak, J., Baek, K., Kwon, H.-A., Yang, J., Park, J., Han, K. M., Kim, B.-R., Shin, H.-W., Choi, H., Lee, E., Chong, J., Cha, Y., Koo, J.-H., Irie, H., Hayashida, S., Kasai, Y., Kanaya, Y., Liu, C., Lin, J., Crawford, J. H., Carmichael, G. R., Newchurch, M. J., Lefer, B. L., Herman, J. R., Swap, R. J., Lau, A. K. H., Kurosu, T. P., Jaross, G., Ahlers, B., Dobber, M., McElroy, C. T., and Choi, Y.: New Era of Air Quality Monitoring from Space: Geostationary Environment Monitoring Spectrometer (GEMS), Bulletin of the American Meteorological Society, 101, E1–E22, https://doi.org/10.1175/BAMS-D-18-0013.1, 2020.

Kreher, K., Van Roozendael, M., Hendrick, F., Apituley, A., Dimitropoulou, E., Frieß, U., Richter, A., Wagner, T., Lampel, J., Abuhassan, N., Ang, L., Anguas, M., Bais, A., Benavent, N., Bösch, T., Bognar, K., Borovski, A., Bruchkouski, I., Cede, A., Chan, K. L., Donner, S., Drosoglou, T., Fayt, C., Finkenzeller, H., Garcia-Nieto, D., Gielen, C., Gómez-Martín, L., Hao, N., Henzing, B., Herman, J. R., Hermans, C., Hoque, S., Irie, H., Jin, J., Johnston, P., Khayyam Butt, J., Khokhar, F., Koenig, T. K., Kuhn, J., Kumar, V., Liu, C., Ma, J., Merlaud, A., Mishra, A. K., Müller, M., Navarro-Comas, M., Ostendorf, M., Pazmino, A., Peters, E., Pinardi, G., Pinharanda, M., Piters, A., Platt, U., Postylyakov, O., Prados-Roman, C., Puentedura, O., Querel, R., Saiz-Lopez, A., Schönhardt, A., Schreier, S. F., Seyler, A., Sinha, V., Spinei, E., Strong, K., Tack, F., Tian, X.,

875   Tiefengraber, M., Tirpitz, J.-L., van Gent, J., Volkamer, R., Vrekoussis, M., Wang, S., Wang, Z., Wenig, M., Wittrock, F., Xie, P. H., Xu, J., Yela, M., Zhang, C., and Zhao, X.: Intercomparison of NO₂, O₄, O₃ and HCHO slant column measurements by MAX-DOAS and zenith-sky UV–visible spectrometers during CINDI-2, Atmos. Meas. Tech., 13, 2169–2208, https://doi.org/10.5194/amt-13-2169-2020, 2020.

Krotkov, N. A., Lamsal, L. N., Celarier, E. A., Swartz, W. H., Marchenko, S. V., Bucsela, E. J., Chan, K. L., Wenig, M., and
880   Zara, M.: The version 3 OMI NO₂ standard product, Atmos. Meas. Tech., 10, 3133–3149, https://doi.org/10.5194/amt-10-3133-2017, 2017.

Lindenmaier, R., Strong, K., Batchelor, R. L., Bernath, P. F., Chabrillat, S., Chipperfield, M. P., Daffer, W. H., Drummond, J. R., Feng, W., Jonsson, A. I., Kolonjari, F., Manney, G. L., McLinden, C., Ménard, R., and Walker, K. A.: A study of the Arctic NOy budget above Eureka, Canada, J. Geophys. Res., 116, n/a-n/a, https://doi.org/10.1029/2011JD016207, 2011.

885   Ma, J. Z., Beirle, S., Jin, J. L., Shaiganfar, R., Yan, P., and Wagner, T.: Tropospheric NO₂ vertical column densities over Beijing: results of the first three years of ground-based MAX-DOAS measurements (2008–2011) and satellite validation, Atmos. Chem. Phys., 13, 1547–1567, https://doi.org/10.5194/acp-13-1547-2013, 2013.

McLinden, C. A., Olsen, S. C., Hannegan, B., Wild, O., Prather, M. J., and Sundet, J.: Stratospheric ozone in 3-D models: A simple chemistry and the cross-tropopause flux, J. Geophys. Res., 105, 14653–14665, https://doi.org/10.1029/2000JD900124,
890   2000.

Moran, M. D., Menard, S., Talbot, D., Huang, P., Makar, P. A., Gong, W., Landry, H., Gong, S., Gravel, S., Crevier, L.-P., and Kallaur, A.: Particulate-matter forecasting with GEM-MACH15, a new Canadian operational air quality forecast model, in 30th NATO/SPS ITM on Air Pollution Modelling and Its Application, 289–293, Springer, San Francisco, 2009.

895   Murray, L. T.: Lightning NO_x and Impacts on Air Quality, Curr Pollution Rep, 2, 115–133, https://doi.org/10.1007/s40726-016-0031-7, 2016.

Nowlan, C. R., Liu, X., Janz, S. J., Kowalewski, M. G., Chance, K., Follette-Cook, M. B., Fried, A., González Abad, G., Herman, J. R., Judd, L. M., Kwon, H.-A., Loughner, C. P., Pickering, K. E., Richter, D., Spinei, E., Walega, J., Weibring, P., and Weinheimer, A. J.: Nitrogen dioxide and formaldehyde measurements from the GEOstationary Coastal and Air Pollution
900   Events (GEO-CAPE) Airborne Simulator over Houston, Texas, Atmos. Meas. Tech., 11, 5941–5964, https://doi.org/10.5194/amt-11-5941-2018, 2018.

Ortega, I., Koenig, T., Sinreich, R., Thomson, D., and Volkamer, R.: The CU 2-D-MAX-DOAS instrument – Part 1: Retrieval of 3-D distributions of NO₂ and azimuth-dependent OVOC ratios, Atmos. Meas. Tech., 8, 2371–2395, https://doi.org/10.5194/amt-8-2371-2015, 2015.

905   Pavlovic, R., Chen, J., Anderson, K., Moran, M. D., Beaulieu, P.-A., Davignon, D., and Cousineau, S.: The FireWork air quality forecast system with near-real-time biomass burning emissions: Recent developments and evaluation of performance for the 2015 North American wildfire season, Journal of the Air & Waste Management Association, 66, 819–841, https://doi.org/10.1080/10962247.2016.1158214, 2016.

Pendlebury, D., Gravel, S., Moran, M. D., and Lupu, A.: Impact of chemical lateral boundary conditions in a regional air
910   quality forecast model on surface ozone predictions during stratospheric intrusions, Atmospheric Environment, 174, 148–170, https://doi.org/10.1016/j.atmosenv.2017.10.052, 2018.

Pinardi, G., Van Roozendael, M., Hendrick, F., Theys, N., Abuhassan, N., Bais, A., Boersma, F., Cede, A., Chong, J., Donner, S., Drosoglou, T., Dzhola, A., Eskes, H., Frieß, U., Granville, J., Herman, J. R., Holla, R., Hovila, J., Irie, H., Kanaya, Y., Karagkiozidis, D., Kouremeti, N., Lambert, J.-C., Ma, J., Peters, E., Piters, A., Postylyakov, O., Richter, A., Remmers, J.,

915   Takashima, H., Tiefengraber, M., Valks, P., Vlemmix, T., Wagner, T., and Wittrock, F.: Validation of tropospheric NO_2 column measurements of GOME-2A and OMI using MAX-DOAS and direct sun network observations, Atmos. Meas. Tech., 13, 6141–6174, https://doi.org/10.5194/amt-13-6141-2020, 2020.

Platt, U. and Stutz, J.: Differential optical absorption spectroscopy: principles and applications, Springer, Berlin, 597 pp., 2008.

Rodgers, C. D.: Inverse methods for atmospheric sounding: Theory and practice, vol. 2, World Scientific, Singapore, ISBN
920   978-981-02-2740-1, 256 pp., 2000.

Rozanov, A., Rozanov, V., Buchwitz, M., Kokhanovsky, A., and Burrows, J. P.: SCIATRAN 2.0 – A new radiative transfer model for geophysical applications in the 175–2400 nm spectral region, Advances in Space Research, 36, 1015–1019, https://doi.org/10.1016/j.asr.2005.03.012, 2005.

925   Stieb, D. M., Burnett, R. T., Smith-Doiron, M., Brion, O., Shin, H. H., and Economou, V.: A New Multipollutant, No-Threshold Air Quality Health Index Based on Short-Term Associations Observed in Daily Time-Series Analyses, Journal of the Air & Waste Management Association, 58, 435–450, https://doi.org/10.3155/1047-3289.58.3.435, 2008.

Sun, K., Zhu, L., Cady-Pereira, K., Chan Miller, C., Chance, K., Clarisse, L., Coheur, P.-F., González Abad, G., Huang, G., Liu, X., Van Damme, M., Yang, K., and Zondlo, M.: A physics-based approach to oversample multi-satellite, multispecies
930   observations to a common grid, Atmos. Meas. Tech., 11, 6679–6701, https://doi.org/10.5194/amt-11-6679-2018, 2018.

Verhoelst, T., Compernolle, S., Pinardi, G., Lambert, J.-C., Eskes, H. J., Eichmann, K.-U., Fjæraa, A. M., Granville, J., Niemeijer, S., Cede, A., Tiefengraber, M., Hendrick, F., Pazmiño, A., Bais, A., Bazureau, A., Boersma, K. F., Bognar, K., Dehn, A., Donner, S., Elokhov, A., Gebetsberger, M., Goutail, F., Grutter de la Mora, M., Gruzdev, A., Gratsea, M., Hansen, G. H., Irie, H., Jepsen, N., Kanaya, Y., Karagkiozidis, D., Kivi, R., Kreher, K., Levelt, P. F., Liu, C., Müller, M., Navarro
935   Comas, M., Piters, A. J. M., Pommereau, J.-P., Portafaix, T., Prados-Roman, C., Puentedura, O., Querel, R., Remmers, J., Richter, A., Rimmer, J., Rivera Cárdenas, C., Saavedra de Miguel, L., Sinyakov, V. P., Stremme, W., Strong, K., Van Roozendael, M., Veefkind, J. P., Wagner, T., Wittrock, F., Yela González, M., and Zehner, C.: Ground-based validation of the Copernicus Sentinel-5P TROPOMI NO_2 measurements with the NDACC ZSL-DOAS, MAX-DOAS and Pandonia global networks, Atmos. Meas. Tech., 14, 481–510, https://doi.org/10.5194/amt-14-481-2021, 2021.

940   Yilmaz, S.: Retrieval of atmospheric aerosol and trace gas vertical profiles using multi-axis differential optical absorption spectroscopy, University of Heidelberg, 2012.

York, D., Evensen, N. M., Martínez, M. L., and De Basabe Delgado, J.: Unified equations for the slope, intercept, and standard errors of the best straight line, American Journal of Physics, 72, 367–375, https://doi.org/10.1119/1.1632486, 2004.

Zhao, X., Griffin, D., Fioletov, V., McLinden, C., Davies, J., Ogyu, A., Lee, S. C., Lupu, A., Moran, M. D., Cede, A.,
945   Tiefengraber, M., and Müller, M.: Retrieval of total column and surface NO_2 from Pandora zenith-sky measurements, Atmos. Chem. Phys., 19, 10619–10642, https://doi.org/10.5194/acp-19-10619-2019, 2019.

Zhao, X., Griffin, D., Fioletov, V., McLinden, C., Cede, A., Tiefengraber, M., Müller, M., Bognar, K., Strong, K., Boersma, F., Eskes, H., Davies, J., Ogyu, A., and Lee, S. C.: Assessment of the quality of TROPOMI high-spatial-resolution NO_2 data products in the Greater Toronto Area, Atmos. Meas. Tech., 13, 2131–2159, https://doi.org/10.5194/amt-13-2131-2020, 2020.

950   Zhao, X., Fioletov, V., Alwarda, R., Su, Y., Griffin, D., Weaver, D., Strong, K., Cede, A., Hanisco, T., Tiefengraber, M., McLinden, C., Eskes, H., Davies, J., Ogyu, A., Sit, R., Abboud, I., and Lee, S. C.: Tropospheric and Surface Nitrogen Dioxide Changes in the Greater Toronto Area during the First Two Years of the COVID-19 Pandemic, Remote Sensing, 14, 1625, https://doi.org/10.3390/rs14071625, 2022.

Zoogman, P., Liu, X., Suleiman, R. M., Pennington, W. F., Flittner, D. E., Al-Saadi, J. A., Hilton, B. B., Nicks, D. K.,
955 Newchurch, M. J., Carr, J. L., Janz, S. J., Andraschko, M. R., Arola, A., Baker, B. D., Canova, B. P., Chan Miller, C., Cohen,
R. C., Davis, J. E., Dussault, M. E., Edwards, D. P., Fishman, J., Ghulam, A., González Abad, G., Grutter, M., Herman, J. R.,
Houck, J., Jacob, D. J., Joiner, J., Kerridge, B. J., Kim, J., Krotkov, N. A., Lamsal, L., Li, C., Lindfors, A., Martin, R. V.,
McElroy, C. T., McLinden, C., Natraj, V., Neil, D. O., Nowlan, C. R., O'Sullivan, E. J., Palmer, P. I., Pierce, R. B., Pippin, M.
R., Saiz-Lopez, A., Spurr, R. J. D., Szykman, J. J., Torres, O., Veefkind, J. P., Veihelmann, B., Wang, H., Wang, J., and
960 Chance, K.: Tropospheric emissions: Monitoring of pollution (TEMPO), Journal of Quantitative Spectroscopy and Radiative
Transfer, 186, 17–39, https://doi.org/10.1016/j.jqsrt.2016.05.008, 2017.